STOCHASTIC SIMULATION OF THE JANUARY 24, 2020 ELAZIĞ-SİVRİCE EARTHQUAKE

by

Şükran Acar

B.S., Civil Engineering, Istanbul Aydin University, 2018

Submitted to Kandilli Observatory and Earthquake Research Institute
in partial fulfillment of the requirements for the degree of
Master of Science

Graduate Program in Earthquake Engineering

Boğaziçi University

2023

ACKNOWLEDGEMENTS

I would like to express my deepest gratitude and wish to convey my deepest appreciation to my supervisor Prof. Dr. Eser Çaktı. Her support, invaluable guidance, and encouragement throughout this study were instrumental in making this study a success. I would like to thank Assist. Prof. Dr. Karin Şeşetyan for contributing to every stage of my thesis. Without her endless support, remarkable patience, and teaching, this thesis would not have been possible. I am deeply appreciative of her assistance not only with thesis work but also with the challenging times in my personal life. It has been a genuine honor and a great pleasure to work with her.

I wish to extend my special thanks to Dr. Aybige Akinci for sharing the Elazığ-Sivrice earthquake slip model with me, which I used in my study. I am thankful to thank my department friends, and especially Nurullah Açıkgöz, for their experiences, knowledge, and moral support during my thesis work.

I am grateful to my dear friends Simge Emir, Elif Naz Akan, İlknur Çulcuoğlu, Ayşe Bilgin, Elif Özdengelen, and Cem Kuter are always with me throughout this study providing me with continuous support and joviality. I would also like to give special thanks to Dr. Aykut Bora for his support and interest during difficult days.

Last but not least, finally, I would like to express my deepest gratitude to each of my valuable family members, especially my mother Peyrüze, my father Ali, my sisters Ayşe, Sevgi, Seven, Hamdiye, Zeynep, Gülşen, Leyla, and Ümran, and my brother Mahmut for their understanding and support. I cannot express in words my gratitude to my little niece Serayi Yağmur Döner, who supported me with her big heart in my difficult moments. I dedicate this study to my dear late father, Ali Acar, who always supported and believed in me. Although he was unable to witness the completion of my thesis, I am deeply grateful for his great trust in me for my entire life.

ABSTRACT

STOCHASTIC SIMULATION OF THE JANUARY 24, 2020 ELAZIĞ-SİVRİCE EARTHQUAKE

This thesis focuses on the application of stochastic ground motion simulation methodology to the 24 January 2020 Mw 6.8 Elazığ-Sivrice earthquake, which occurred on the Pütürge segment of the East Anatolian Fault in Turkey. In this context, the dynamic corner frequency-based stochastic finite fault method was used to simulate the ground motion fields generated by the 24 January 2020 Elazığ-Sivrice earthquake earthquake. Input parameters for the simulations are derived from regional sources and seismic parameters to ensure the reliable production of synthetic ground motions. The model parameters are evaluated by comparing the real records of the Elazığ-Sivrice earthquake with synthetic records and preferred models are selected accordingly. Moreover, the synthetic records have been compared with regionally suitable ground motion models (GMMs). The stochastic ground motion simulation methodology is used together with the extended fault model, evaluating both random and earthquake specific slip distribution options. Alternative models or values are considered for the stress drop, geometric spreading, Q and duration models as well as for site amplification. A combination of models that yield the lowest error terms both in frequency and time domain parameters is proposed as the preferred model for this study. As a result of this study, it is seen that the simulations of the Elazığ-Sivrice (Mw 6.8) event give reasonable results for frequency ranges higher than 1 Hz and the determined parameters can be further developed and used as input to other studies evaluating seismic hazards in related regions.

ÖZET

24 OCAK 2020 ELAZIĞ-SİVRİCE DEPREMİ STOKASTİK SİMÜLASYONU

Bu tez, Türkiye'de Doğu Anadolu Fayı'nın Pütürge segmentinde meydana gelen 24 Ocak 2020 Mw 6.8 Elazığ-Sivrice depremine stokastik yer hareketi simülasyon metodolojisinin uygulanmasına odaklanmaktadır. Bu kapsamda 24 Ocak 2020 Elazığ-sivrice depreminin oluşturduğu yer hareketi alanlarının simüle edilmesi için dinamik köşe frekansı tabanlı stokastik sonlu fay yöntemi kullanılmıştır. Simülasyonlara yönelik girdi parametreleri, sentetik yer hareketlerinin güvenilir şekilde üretilmesini sağlamak için bölgesel kaynaklardan ve sismik parametrelerden türetilmektedir. Elazığ-Sivrice depreminin gerçek kayıtları sentetik kayıtlarla karşılaştırılarak model parametreleri değerlendirilmiş ve tercih edilen modeller buna göre seçilmiştir. Ayrıca sentetik kayıtlar bölgesel olarak uygun yer hareketi modelleri (GMM) ile karşılaştırılmıştır. Stokastik yer hareketi simülasyon metodolojisi, genişletilmiş fay modeliyle birlikte kullanılarak hem rastgele hem de depreme özgü kayma dağılımı seçeneklerini değerlendirmektedir. Gerilim düşüşü, geometrik yayılma, Q ve süre modelleri ile saha büyütmesi için alternatif modeller veya değerler dikkate alınır. Bu çalışma için tercih edilen model olarak hem frekans hem de zaman alanı parametrelerinde en düşük hata terimlerini veren modellerin bir kombinasyonu önerilmiştir. Bu çalışma sonucunda Elazığ -Sivrice (Mw 6.8) depreminin simülasyonlarının 1 Hz'den yüksek frekans aralıkları için makul sonuçlar verdiği ve belirlenen parametrelerin daha da geliştirilerek ilgili bölgelerdeki sismik tehlikeleri değerlendiren diğer çalışmalara girdi olarak kullanılabileceği görülmektedir.

TABLE OF CONTENTS

LIST OF FIGURES

LIST OF TABLES

LIST OF SYMBOLS

E	EW Component
f	Frequency
I_0	Epicentral Intensity
I	Intensity
L	Fault Length
M_w	Moment Magnitude
N	NS Component
Q_f	Frequency Dependent Quality Factor
R	Source to Site Distance
R_{epi}	Epicentral Distance
R_{jb}	Joyner–Boore Distance
R_{rup}	Rupture Distance
T_0	Source Duration
$Vs30$	Time-Averaged Shear-Wave Velocity to 30m Depth
W	Fault Width
$Z(R)$	Geometric Spreading
$\Delta\sigma$	Stress Drop

LIST OF ACRONYMS/ABBREVIATIONS

AFAD	Disaster and Emergency Management Authority
EMSC	European-Mediterranean Earthquake Catalogue
EW	East West
FAS	Fourier Amplitude Spectra
GMMs	Ground Motion Models
GFZ	German Research Centre for Geosciences
INGV	The National Institute of Geophysics and Volcanology
KOERI	Kandilli Observatory And Earthquake Research Institute
Lat	Fault Length
Lon	Fault Length
Mag	Magnitude
MTA	Mineral Research and Exploration General Directorate
NAF	North Anatolian Fault
NAFZ	North Anatolian Fault Zone
NEHRP	National Earthquake Hazards Reduction Program
NS	North South
Obs	Observed
PGA	Peak Ground Acceleration
PGV	Peak Ground Velocity
QTM	Quaternary, Tertiary, Mesozoic
Syn	Synthetic
USGS	United States Geological Survey

1. INTRODUCTION

1.1. General

Natural disasters, such as earthquakes, are considered to be among the most devastating phenomena that may lead to substantial losses of life and property. This destructive natural phenomenon is among the study areas of many disciplines such as civil engineering, structural engineering, earth sciences, the insurance industry, and public policy. Especially for engineering objectives, the subject of strong ground motion, i.e. the ground motion caused by the propagation of the waves generated by earthquake ruptures is extensively studied to assess and mitigate the potential impacts of earthquakes on structures, thereby minimizing losses and mitigating earthquake risks.

Earthquake strong ground motion recordings are not abundantly available, yet, for several regions of the world. For such regions for which earthquake-related studies necessitate the use of time histories or parameters derived from such time histories (e.g. peak ground motion parameters), various solutions are proposed. Although using recorded ground motions from comparable regions with similar tectonic and site conditions is a solution, ground motion simulation is a well-accepted alternative method used to estimate the required characteristics of ground motions in such regions. At the same time, the simulations are also valuable for seismically active regions with extensive and comprehensive data sets, as they comprise information on earthquake physics, seismic parameters, and faulting mechanisms and can be used to estimate the entire wave field caused by an earthquake rupture.

Simulation techniques are actively and widely used by seismologists and earthquake engineers in strong ground motion prediction studies. The frequency range of the resulting waveforms are of particular importance as different techniques are used for low- (e.g. $< 1Hz$) and high-frequency parts of the spectrum. There are several com-

mon methods for simulating the high-frequency content of the strong motion such as stochastic simulation technique (SST), composite source modeling technique (CSMT), empirical Green's function technique (EGFT), and semi-empirical technique (SET). Additionally, as a hybrid approach, a combination of empirical Green's function and stochastic is used [1].

In this thesis, the stochastic finite-fault simulation method with a dynamic corner frequency model is employed to simulate the 24.01.2020 Mw 6.8 Elazığ-Sivrice earthquake that occurred in the East Anatolian Fault Zone. Available regional data and models are used and results are critically evaluated to ensure that reliable synthetic time histories are produced. Model parameters were validated by comparing synthetic ground motions with those recorded during the Elazığ-Sivrice earthquake. Additionally, the ground motion parameters obtained from the simulation model were compared with regionally applicable ground motion models (GMMs).

1.2. Literature Survey

Simulation of the earthquake ground motion has been a subject of extensive research in both earth sciences and engineering disciplines. These simulations play a crucial role in understanding earthquake physics, faulting mechanisms, and seismic parameters, as well as estimating ground motions at locations with sparse seismic data. In addition, it allows a comprehensive understanding of earthquake phenomena and contributes significantly to seismic hazard assessment and risk mitigation efforts.

Stochastic simulation, also known as probabilistic simulation, is a powerful technique widely used in various fields to model and analyze complex systems or processes that involve uncertainty. Engineering seismology is one of the disciplines in which stochastic simulation is widely used and stochastically simulated acceleration time histories provide valuable insights in understanding the characteristics and in predicting ground shaking caused by earthquakes.

A literature review of stochastic ground motion simulation methods reveals several key developments and applications:

The fundamentals of stochastic ground motion simulations are laid out by superimposing random amplitudes and durations with random time delays to simulate mid and high frequencies, and as such they are complementary to deterministic ground motion simulations that can only be used for low frequencies [2–4]. Subsequently, Aki [5] made significant improvements by defining the change with time of the earthquake-induced displacement, in relation to the "source spectrum" and the velocity function. This w^{-2} model, which showed a decrease in the source spectrum amplitudes with the square of the frequency, proved to be a physically reasonable model for the high-frequency part of the earthquake time histories. Building on Aki's work, researchers such as Hanks and McGuire [6], Boore [7], and Silva [8] have proposed deterministic stochastic models in which earthquake records are represented as stochastic events over time with Fourier amplitude spectra determined by seismological models of the source, path, and site effects.

The "source spectrum" proposed by Aki [5] as a new method and the study of Hanks and McGuire [6] were combined by Boore [7] to obtain time-domain ground motion simulations. This approach provided a better representation of fault rupture and seismic wave propagation. Beresnev and Atkinson [9] extended the methodology to incorporate the issue of fault dimensions and thus the stochastic finite fault methodology has emerged. In this approach, instead of considering a single point source (which is not in fact applicable to large-magnitude events), an extended rupture surface corresponding to the magnitude of the event is modeled via small sub-faults, each being treated as an individual point source. Each sub-fault was assigned a specific location, and the seismic waves generated from each sub-fault were superimposed and combined in the time domain with the overall impact of the whole rupture on ground motion. Motazedian and Atkinson [10] made important improvements to the methodology developed by Beresnev and Atkinson [9]. The so-called "dynamic corner frequency" method, in which the corner frequency changes with time and position, significantly increased the

accuracy and reliability of simulations and provided a more realistic representation of ground motion at different stages of earthquake rupture.

The approach has been extensively validated through various studies in Turkey. Yalçınkaya [11] validated the stochastic method by investigating the 1998 Ceyhan earthquake, while Uğurhan and Askan [12] and Karimzadeh et al. [13] examined the 1999 Düzce earthquake. Askan et al. [14] studied the 1992 Erzincan earthquake, and Akinci and Antonioli [15], as well as Zengin and Çaktı [16], conducted studies on the 2011 Van earthquake, all used the stochastic method and validated its accuracy with the characteristics of the earthquake they examined.

1.3. Objective and Scope

This study employed the dynamic corner frequency-based stochastic finite fault method developed by Motazedian and Atkinson [10] to simulate the ground motions generated by the 24.01.2020 Elazığ-Sivrice earthquake. The primary purpose of this thesis is to acquire a plausible and realistic synthetic strong ground motion field by using the simulation model developed for the region and the specific earthquake under study. For this purpose, the input parameters for the simulations are derived from regional sources and seismic parameters to ensure reliable production of synthetic ground motions. The model parameters are validated by comparing the real records of the Elazığ-Sivrice earthquake with synthetic records. Moreover, the synthetic records have been compared with regionally suitable GMMs. All simulations were performed using the finite fault model and stochastic modeling using the EXSIM [10], [17] program. The outputs of simulations were visualized with MATLAB software and some maps in the thesis were produced using ArcGIS Pro software.

In Chapter 2, the principles of the stochastic strong ground motion simulation method, which is the simulation technique that forms the basis of the thesis, are introduced. The methodology employed in this study comprises two main approaches: the stochastic point-source and the stochastic finite-fault simulation approach. These

techniques were comprehensively explained and detailed in the following sections, emphasizing their basic principles and application steps.

In Chapter 3, first, the seismological characteristics of the main event are presented. In the first part of the study, background information about the Elazığ region is given. Then, the observed strong ground motion data are presented. Following this, the regional model parameters are validated by the strong ground motion records of the Elazığ-Sivrice earthquake. Furthermore, this chapter includes a comprehensive comparison between the synthetic and observed records and GMMs.

Finally, Chapter 4 provides a summary of the results obtained in this thesis together with a set of recommendations for future research.

2. METHODOLOGY OF STOCHASTIC STRONG GROUND MOTION SIMULATION

2.1. Overview of the methodology

In this chapter, the stochastic strong ground motion simulation methodology used to simulate the ground motions of the 24.01.2020 Elazığ-Sivrice earthquake is presented. The methodology consists of two essential approaches: the stochastic point source and the stochastic finite-fault simulation method.

Section 2.2 focuses on the stochastic point-source simulation technique in detail and presents its underlying theory. In this method, a simplified seismic source is considered as a single point and the random nature of ground motion is considered. This section provides detailed information about the models for source, path, and site, allowing both an understanding of the required input parameters for each component and an in-depth understanding of the simulation methodology.

Section 2.3 introduces finite-fault simulation modeling, which provides a more realistic representation of earthquake sources by considering the rupture process and its effects on ground motion. This section emphasizes the significance of the static and dynamic corner frequency approaches, as they are important in accurately capturing the frequency characteristics of the synthetic time histories.

Finite fault modeling focuses on the spatial extent and complexity of the seismic source by modeling rupture along a finite fault surface. This method allows for considering slip distribution, fault geometry, and rupture propagation.

Here we should also emphasize that the simulation methodology relies on appropriate input parameters and models for accurate results. Validation against observed data is crucial to ensure the reliability and validity of the simulated ground motions.

Reliable ground motion time histories obtained via this methodology may be crucial in assessing the seismic hazard, evaluating the structural response, and informing engineering design.

2.2. Stochastic Point Source Method

Hanks and McGuire [6] were the pioneers who brought forth the concept of incorporating stochastic parameters into ground motion simulations. By acknowledging the complex nature of high-frequency ground motions, they proposed the use of stochastic methods to account for the random phase angles that contribute to this complexity.

Their groundbreaking contribution shed light on the necessity of considering the random nature of ground motions. It catalyzed the development and application of stochastic methods in seismic engineering.

Unlike deterministic modeling methods, stochastic point-source modeling incorporates stochastic parameters to account for the variability and complexity of ground motions, particularly at high frequencies.

Their complex character characterizes the high-frequency part of strong ground motions ($f > 1\,\mathrm{Hz}$). It can be said that this complexity is due to the loss of phase coherence between stations close to each other. Because of the complex phase inconsistency, deterministic methods have to be adapted to high frequencies to simulate ground motions. One or more stochastic parameters are required to model high-frequency strong ground motions that describe random phase angles [6]. This methodology has been proven valuable in improving the accuracy of ground motion simulations, particularly at frequencies greater than 1 Hz.

The point-source part of the stochastic simulation methodology aims to produce a time series that is stochastic in character, while its spectrum accurately indicates a predetermined deterministic spectrum for a specific point source. The construction of

this time series starts with the generation of a band-limited Gaussian white noise with zero mean and variance, which is associated with the seismic magnitude and source and site distance. The noise then has been windowed to limit its duration and converted into the frequency domain using a transformation method, such as the Saragoni-Hart method [18]. This transformation allows for the representation of the time series in terms of its frequency components. To normalize windowed noise, it is multiplied by the square root of the mean square amplitude spectrum. This normalization step ensures that the resulting time series has the desired properties and accurately represents the specified deterministic spectrum for the given point source. The resulting spectrum is multiplied by the theoretical S wave amplitude spectrum. The final step involves the inverse Fourier transformation which is performed to obtain the stochastic acceleration in the time domain from the modified spectrum. As a result of these steps, a time series with a finite duration with a specific amplitude spectrum is produced. This amplitude spectrum expresses its path and site effects.

A detailed illustration of the procedures is presented in Figure 2.1. In equation 2.1 introduced by Boore [19], the ground motion amplitude spectrum in the stochastic point-source method is given. In this equation, the multiplier filter functions are E (source spectrum), P (path effect), G (site effects), and I (instrument response) giving the Fourier Amplitude Spectrum of a seismic signal as:

$$Y(M_0, R, f) = E(M_0, f) \cdot P(R, f) \cdot G(f) \cdot I(f) \tag{2.1}$$

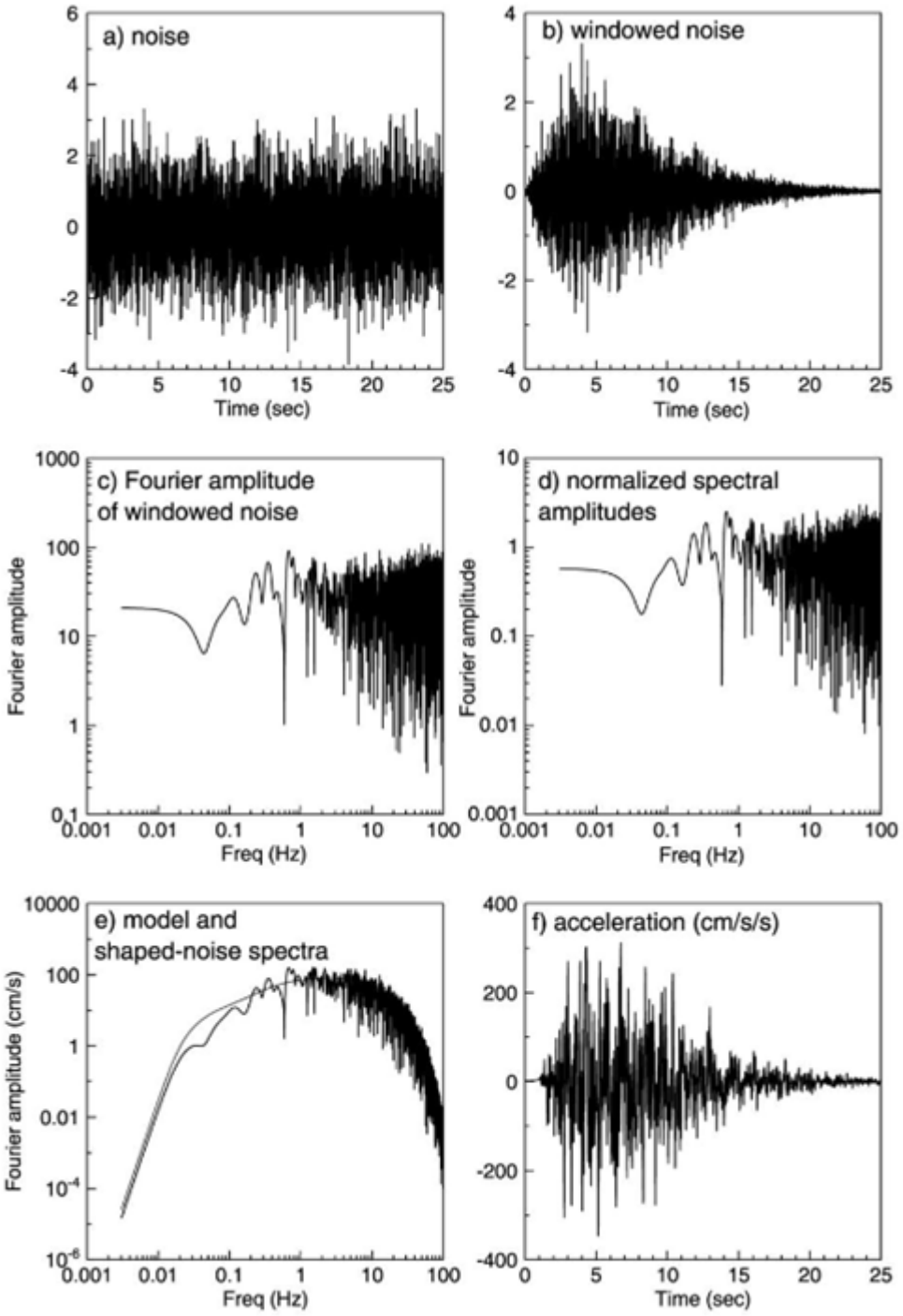

Figure 2.1. The steps of the stochastic point-source modeling procedure as defined by Boore [19].

2.2.1. Source Spectrum

Source effects include parameters of a rupture process on a fault plane, where fault dimensions and orientation are specified. Source effects are modeled using mathematical representations or empirical relationships that describe the behavior of the earthquake source. Within these models, physical properties like earthquake magnitude, depth of the fault, types of faults, slip distribution, rupture velocity, and stress drop vary randomly over the fault surface. This approach allows for more realistic representations of actual rupture behavior with random variations. Therefore, it can capture the heterogeneous nature of fault slip and rupture velocity, allowing a more accurate simulation of ground motion to be obtained.

In stochastic ground motion simulations, the source function is derived from the solution of Green's function, which describes the far-field shear wave displacement caused by a point shear dislocation in a homogeneous, isotropic, unbounded medium and is as follows:

$$u(x,t) = \frac{\Re^{\theta\gamma}}{4\pi\rho\beta^3 R} M'(t)\left(t - \frac{R}{\beta}\right) \tag{2.2}$$

In this equation, $u(x,t)$ denotes the dynamic displacement, $\Re^{\theta\gamma}$ and β are the radiation pattern and the shear-wave velocity, respectively. While R is the from source to site distance, $M'(t)$ represents the moment rate function [20].

In general, the seismic moment is introduced as the product of the shear modulus μ, the source time function $\bar{u}(t)$, and the dislocation area (A).

$$M(t) = \mu\bar{u}(t)A \tag{2.3}$$

The source time function is one of the significant uncertainties in earthquake source modeling. It is expressed as the dynamic change in the amplitude of the forcing

function acting on the fault plane during an earthquake. Several models have been suggested to represent the source time function, each with its assumptions and uncertainties. The particle displacement increases with time and to represent this increase a ramp function and a step function are used by Haskell [21] and Aki [5] respectively.

In stochastic simulation modeling, the source time function is established following Brune's framework [22], which represents the dislocation in terms of the effective stress driving the movement along both sides of the rupture surface. This formulation is then improved by Beresnev and Atkinson [9] to ensure that the boundary conditions are appropriately satisfied. These modifications enhance the accuracy and reliability of the stochastic point-source methodology in modeling seismic sources.

In stochastic modeling, the source-time function and the velocity function are as follows:

$$\bar{u}(t) = \frac{\sigma}{\mu}\beta\tau\left[1 - \left(1 + \frac{t}{\tau}\right)e^{-\frac{t}{\tau}}\right] \tag{2.4}$$

$$\bar{u}'(t) = \frac{\sigma}{\mu}\beta(\frac{t}{\tau})\left(e^{-\frac{t}{\tau}}\right) \tag{2.5}$$

Thus, equation (2.2) representing the far-field shear wave displacement is rewritten as follows:

$$u(x,t) = \frac{\Re^{\theta\gamma}M_0}{4\pi\rho\beta^3 R}\left(\frac{t-\frac{R}{\beta}}{\tau}\right)e^{\frac{[t-\frac{R}{\beta}]}{\tau}} \tag{2.6}$$

By Fourier transformation of Equation (2.6), the following is obtained:

$$u(x,\omega) = \frac{\Re^{\theta\gamma} M_0}{4\pi\rho\beta^3 R} \left(\frac{1}{1 + \left(\frac{\omega}{\omega_c}\right)^2} \right) \tag{2.7}$$

Brune [22, 23] defines the corner frequency ($fc = \omega c/2\pi$) as:

$$fc = 4.9 \cdot 10^6 \beta_s \left(\frac{\Delta\sigma}{M_0} \right)^{1/3} \tag{2.8}$$

In this equation, fc represents the corner frequency in Hz, β_s represents the shear wave velocity in km/s, $\Delta\sigma$ expresses the stress drop in bars, M_0 represents the seismic moment in dyne-cm. Equations 2.7 with 2.8 come together to form the source function, and the general form of the source function can be written as follows:

$$E(M_0, \omega) = C \cdot M_0 \cdot S(\omega, \omega_c) \tag{2.9}$$

C representing a scaling constant is defined as:

$$C = \frac{\Re^{\theta\gamma} \cdot FS \cdot PRTITN}{4\pi\rho\beta^3 R} \tag{2.10}$$

In this equation, the variables, respectively, are defined as $\Re^{\theta\gamma}$is expressed as the radiation pattern and is used as 0.55 for shear waves. FS is the amplification factor on the free surface, generally used to be 2. $PRTITN$ is defined as a reduction factor mostly considered $1/\sqrt{2}$. The density is represented by ρ and the shear wave velocity is represented by β.

M_0 is the seismic moment of the earthquake defined in Equation 2.3. The moment magnitude (M) estimated based on the seismic moment (M_0) was defined by Hanks

and Kanamori [24] and is as follows:

$$M = \frac{2}{3} log(M_0) - 10.73 \tag{2.11}$$

Eventually, the source displacement spectrum is:

$$S(\omega, \omega_c) = \frac{1}{1 + (\frac{\omega}{\omega_c})^2} \tag{2.12}$$

The source modeling is the weakest part of stochastic modeling since it has limitations in accurately representing the complex behavior of earthquake sources. It has been observed that this model works limitedly, especially for low frequencies. However, since low frequencies are not critical for engineering purposes, the frequency band simulated by the stochastic approach is considered useful.

2.2.2. Path Effects

It can be said that the path effect is the second important factor altering the properties of ground motion records. As seismic waves travel through the ground, changes are introduced in their frequency content, amplitude, duration, and velocity. There are two types of path effects: geometric and anelastic attenuation. Geometric propagation, also known as the elastic process, reduces ground motion amplitudes as seismic wave energy spreads over an increasingly larger area. Anelastic attenuation is defined by Romero and Rix [25] as the dissipation of seismic energy. Anelastic attenuation corresponds to an inelastic process resulting in the dissipation of seismic energy. Geometric diffusion represents an elastic process that conserves seismic energy.

The path effect filter defined by Boore [19] gives the geometrical and anelastic attenuation and is as in Equation 2.13.

$$P(R, w) = Z(R) \cdot e^{-\frac{\pi f R}{Q(f) \cdot \beta}} \tag{2.13}$$

In this equation, R, $Z(R)$, and $Q(f)$ indicate the distance source-site, geometrical spreading function, and a frequency-dependent quality factor, respectively.

In this section, the three essential parameters of the path effect function are described: geometric spreading, quality factor, and duration.

$Z(R)$, which indicates the geometrical spreading function, is a mathematical function that describes how the amplitude of seismic waves changes with distance from the earthquake source. The $Z(R)$ represents a piecewise continuous function since it consists of different segments or regions, each corresponding to a certain distance from the source. The $Z(R)$ function described by Boore (2003) is as follows:

$$\begin{cases} \frac{R_0}{R}, & R \leq R_1 \\ Z(R_1)\left(\frac{R_1}{R}\right) p_1, & R_1 \leq R \leq R_2 \\ Z(R_n)\left(\frac{R_n}{R}\right) p_n, & R \geq R_n \end{cases} \tag{2.14}$$

In the equation, R is the distance from the epicenter to the observation point.

In Equation 2.13, the term $e^{-\frac{\pi f R}{Q(f)\cdot\beta}}$ denotes anelastic attenuation.$Q(f)$ represents the quality factor that is dependent on frequency. The quality factor, also known as the anelastic attenuation term, is a parameter that describes the energy loss or damping of seismic waves as they propagate through is not completely elastic Earth. Since the specific value of the quality factor varies from region to region, a quality factor suitable for the seismic region studied should be selected. If a suitable quality function is not available in the literature, regional seismic data can be used to derive quality factor models [20].

The quality factor can be defined as:

$$Q = Q_0 \cdot f^n \tag{2.15}$$

Q_0 in the equation represents the heterogeneous behavior of the Earth's environment, while the parameter "n" is a parameter that varies according to the region [26]. Accurate estimation of the quality factor is crucial to obtaining realistic high-frequency ground motion spectra [27]. It provides to comprehend the effects of anelastic losses and allows ground motion simulations and seismic hazard assessments to better represent the actual seismic behavior in a given area. Another parameter in path effects is distance-dependent time. The distance-dependent time indirectly affects the deterministic target spectrum (Equation 2.7). However, since the peak amplitudes decrease with increasing time, the distance-dependent time is necessary for the time domain projection. The duration function is as follows:

$$T = T_0 + bR \tag{2.16}$$

In this equation, T_0 is the source duration, b denotes the slope of the distance-dependent duration term, and R represents the distance from the source to the site. T_0 increases with the magnitude of the earthquake and is inversely proportional to the corner frequency since $T_0 = 1/(2f_c)$ [9].

Identifying regional models for geometric spreading, quality factor, and duration requires careful analysis and validation using observed ground motion data. A comparison should be made between synthetic and recorded ground motions when making choices regarding path characteristics. By making these comparisons and improving the simulation parameters, an optimal match between observed and simulated ground motions can be obtained. This iterative process allows one parameter to be changed while keeping the others constant, which helps determine optimal values for simulation. When determining the optimum simulation parameters, the FAS of the synthetic and observed ground motions is usually compared. In summary, identifying regional models for synthetic ground motion involves a rigorous analysis of regional datasets, iterative comparison with observed data, and optimization to obtain the best fit between simulated and recorded ground motions.

2.2.3. Site Effects

Site effects express the phenomenon in which the characteristics of seismic waves (amplitude, duration, and frequency content) are modified as they pass through or interact with the geological and geomorphological features of a specific site.

Soil density and velocity generally tend to decline from the bedrock to the ground level. Seismic impedance decreases due to the movement of seismic waves, and wave amplitudes tend to increase in order to conserve this decrease, that is, elastic energy [28]. Meanwhile, wave amplitudes decrease because of the damping effect in soft soil layers. After all, site effects include both amplification and reduction of waves. Understanding site effects is crucial in accurately assessing seismic hazards.

One way to quantify site effects is through the site response function, often denoted as $G(f)$. Mathematically, the site response function $G(f)$ can be expressed as the product of two functions as in the following :

$$G(f) = A(f) \cdot D(f) \tag{2.17}$$

In this equation, $A(f)$ and $D(f)$ represent the amplification, and the diminution functions, respectively.

2.2.3.1. Amplification Function. Determining soil properties and evaluating site amplification is a fundamental aspect of the earthquake simulation process. Various techniques are employed for modeling site effects, with theoretical transfer functions being highly effective when detailed soil velocity profiles are available. These profiles are usually obtained through methods like boreholes, seismic reflection, and refraction, but these techniques can be complex and expensive, particularly for deep sites.

When it comes to site amplification calculations, the methodology chosen depends on whether the site's velocity profile is known. Site-specific velocity profiles provide

more accurate results but can be challenging and costly to determine. Consequently, empirical approaches may be preferred in certain situations.

Two primary theoretical methods for estimating site amplification include theoretical site response analyses and the quarter-wavelength method. The more widely used empirical method is the Horizontal Vertical Spectral Ratio (HVSR or H/V) technique introduced by Nakamura [29]. The second method was introduced by Boore and Joyner [30], which allows a practical prediction of site amplification in the quarter wavelength method. In this approach, amplification factors are introduced for each frequency by taking into account the ratio of the seismic impedance at the source level to the mean seismic impedance at a certain depth.

The equation is as follows:

$$A(f(z)) = \sqrt{\frac{\rho_s \beta_s}{\bar{\rho}(z)\bar{\beta}_s(z)}} \tag{2.18}$$

In this equation, $f(z) = \frac{1}{4S_{tt}(z)}$ represents the frequency corresponding to depth z and $S_{tt}(z)$ is the S-wave travel time from depth z to the ground; ρ_s and $\bar{\rho}(z)$ indicate the density and travel-time-weighted average of density, respectively; β_s and $\bar{\beta}_s(z)$ denote S-wave velocity around the source and S-wave velocity to depth z.

The quarter-wavelength method has been performed versus theoretical amplifications and verified its accuracy study (e.g., [30,31]), in particular, involved applying this method to representative soil profiles, resulting in the derivation of generic site amplification functions tailored to the National Earthquake Hazards Reduction Program (NEHRP) 2009 soil classes. These functions are particularly valuable when detailed soil profile data for a specific site are unavailable. In such cases, even with some degree of uncertainty, these generic amplification functions can still be applied, providing essential insights into site-specific seismic response characteristics.

Nakamura's [29] H/V spectral ratio approach is another widely used empirical

method to estimate site amplification factors. It operates on the principle that local site effects primarily affect horizontal ground motion components, while vertical components remain relatively unaffected. This method allows the determination of site-specific amplification factors by comparing the spectral acceleration between horizontal and vertical ground motion. It's particularly useful when site velocity profiles are unavailable, providing a practical alternative to theoretical methods. However, in cases with limited or incomplete data, the method may introduce uncertainties.

2.2.3.2. Diminution Function. In near-field conditions, there is a notable rapid decay in high-frequency spectral values, and this diminution effect is distinct from wave propagation attenuation [7]. There are different opinions about the primary cause of this high-frequency decay, with some attributing it to source properties and others to site effects. Papageorgiou and Aki [32] suggest that the reduction in high frequencies is linked to earthquake source processes, whereas Hanks [33] and Atkinson [34] associate this phenomenon with attenuation in near-surface soil layers. To model this decay, two fundamental approaches are employed: fmax and kappa. F_{max} , introduced by Hanks [33], sets a cutoff frequency for the seismogram, and the corresponding diminution factor is defined as follows:

$$D(f) = \left(1 + (\frac{f}{f_{max}})^8\right)^{-0.5} \tag{2.19}$$

The kappa parameter, developed by Anderson and Hough [35], offers a second method to model high-frequency spectral attenuation in seismic ground motion records. This approach characterizes the attenuation of ground motion at high frequencies through an exponential function. It calculates vertical and horizontal kappa values to represent this attenuation. The process begins with the generation of Fourier acceleration spectra for each component of ground motion, plotted on a semi-logarithmic scale. A linear fit is applied to identify the decay portion of the log amplitudes in these spectra. The kappa factors for each component are derived by dividing the slope of the best-fit line by pi. This calculation is essential for accurately analyzing the data

and drawing meaningful conclusions. These calculated kappa values are then plotted against the epicentral distances of the stations. Through a linear regression analysis, the ordinate of the best-fit line gives zero-distance kappa (κ_0) value. κ_0, which reflects near-surface attenuation, is used in stochastic modeling to account for distance effects between the earthquake source and the recording station, and its function is given as follows:

$$D(f) = e^{-\pi\kappa_0 f} \tag{2.20}$$

2.3. Stochastic Finite-Fault Method for Extended Ruptures

The stochastic finite-fault methodology [9] is a powerful method, particularly for large magnitude events or for the simulation of the wave field in regions close to the earthquake rupture, i.e. for cases where the fault dimensions become important. This approach extends the original point-source models and becomes necessary when observation points are situated closer to the fault plane, requiring consideration of finite-fault effects.

To simulate these effects, as introduced in the work of Hartzell [36], the extended rupture plane is divided into a regular grid of smaller fault sections, which are termed as sub-faults and each sub-fault is treated as a stochastic point source. The contributions from these sub-faults are superimposed in the time domain to obtain the resulting ground motion accelerogram. This technique assumes that the hypocenter is situated at the center of one of the sub-faults, the location of which is given as an input parameter. The rupture begins at the hypocenter and propagates in all directions at a constant shear wave velocity. The propagation continues kinematically until it reaches all sub-faults. This computation involves summing up the contributions from each sub-fault along both dimensions of the rupture surface and the ultimate response of the whole

fault plane is obtained as presented by the equation below [37]:

$$a(t) = \sum_{i=1}^{nl} \sum_{j=1}^{nw} a_{ij} \cdot (t - \Delta t_{ij} - T_{ij}) \tag{2.21}$$

Here, $a(t)$ denotes the acceleration value at investigation point at time t. Summation is performed over both dimensions of the rupture plane, nl representing the number of sub-faults along the length and nw the number of sub-faults along the width. $a_{ij}(t)$ corresponds to the ground acceleration of the ijth sub-fault, which is now considered as a point source following the definition by Boore [7]. Δtij signifies the delayed time of the radiated wave from the ijth sub-fault to the station. Figure 2.2 illustrates the evolution of the rupture over the fault plane.

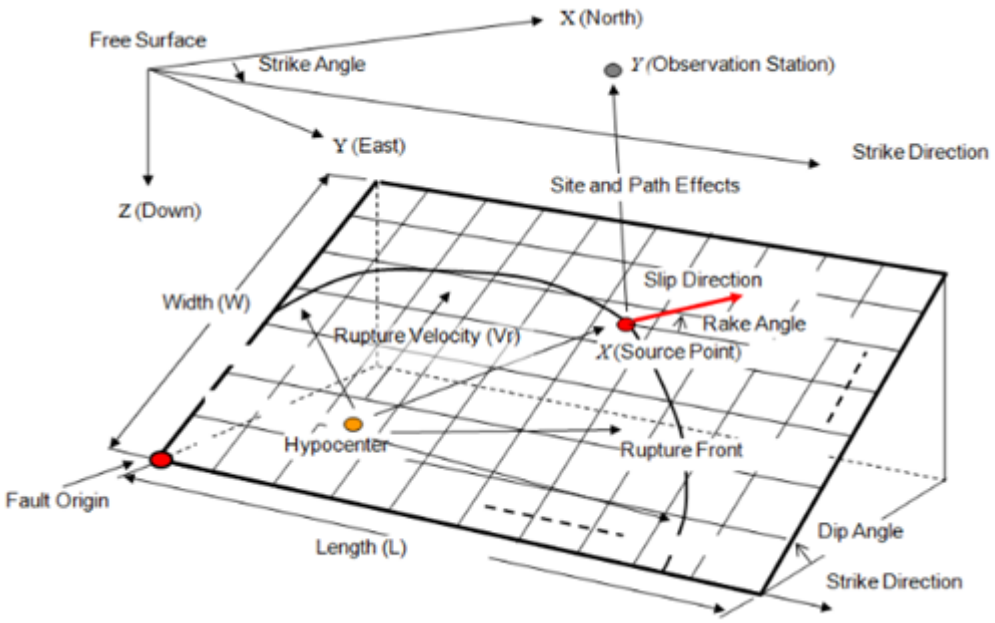

Figure 2.2. Fault rupture plane geometry [38]

For the simplest extended rupture case, a uniform slip distribution is assumed and the representation of the seismic moment is defined for the sub-faults:

$$M_{0ij} = \frac{M_0}{N} \tag{2.22}$$

In this approach, the seismic moment is denoted as M_0 and N stands for the number

of sub-faults involved in the simulation. When slip on the sub-faults deviate from uniformity, the calculation of the seismic moment for sub-faults incorporates the weight of the slip associated with that particular sub-fault [39]. The seismic moment under these conditions can be expressed as:

$$M_{0ij} = \frac{M_0 \cdot S_{ij}}{\sum_{i=1}^{nl} \sum_{j=1}^{nw} S_{kl}} \tag{2.23}$$

Here, $S_{i,j}$ represents the relative slip weight of sub-faults.

In the study of [9], the acceleration spectrum corresponding to each sub fault ($A_{i,j}$) was treated as resulting from a point source rupture as given in the following equation:

$$A_{ij}(f) = C \cdot M_{0ij} \frac{(2\pi f)^2}{[1 + (f_{0ij})^2]} \frac{1}{R_{ij}} \exp\left(-\frac{\pi f R_{ij}}{Q(f)\beta}\right) \exp(\pi f \kappa) A(f) \tag{2.24}$$

The spectrum's characteristics, particularly the static corner frequency $f_{c,i,j}$, were given as:

$$f_{cij} = 4.9 \cdot 10^6 \cdot \beta \left(\frac{\Delta\sigma}{M_{0ij}}\right)^{1/3} \tag{2.25}$$

The original FINSIM program, proposed by Bresnev and Atkinson [9], implemented this methodology. However, it had limitations concerning sub-fault size and number, affecting the resulting synthetic ground motions. These disadvantages were overcome by Motazedian and Atkinson [10] in the updated EXSIM program. They introduced the so-called "dynamic corner frequency" method, where the corner frequency is inversely proportional to the area of ruptured sub-faults at any given time. This ensures the corner frequency decreases with increasing duration and conserves

radiated energy at higher frequencies and is given as:

$$f_{cij} = N_R(t)^{-1/3} \cdot 4.9 \cdot 10^6 \cdot \beta \left(\frac{\Delta\sigma}{M_{0_{ave}}} \right)^{1/3} \tag{2.26}$$

In this equation, $N_R(t)$ represents the total number of ruptured sub-faults at time t, while $M_{0_{ave}}$ denotes the average seismic moment of sub-faults equal to M_0/N.

Significant improvements to the method have later been introduced by Motazedian and Atkinson [10]. Their introduction of the "pulsing area percentage" concept improved the approach by distinguishing sub-faults as being part of the passive or active rupture areas based on the ratio of ruptured (active) area to the entire fault area. This approach lead to a reduction in dynamic corner frequency and radiated energy at higher frequencies until the specified pulsing area percentage was reached. Once the pulsing area percentage is attained, the dynamic corner frequency becomes stable, ensuring the model's accuracy. To address the declining radiated energy issue, a scaling factor H_{ij} was introduced to balance the high-frequency spectral levels of sub-faults:

$$H_{ij} = \left\{ N \frac{\Sigma \left[\frac{f^2}{1+\left(\frac{f}{f_0}\right)^2} \right]}{\Sigma \left[\frac{f^2}{1+\left(\frac{f}{f_{0ij}}\right)^2} \right]} \right\} \tag{2.27}$$

The stress drop value and pulsing area percentage value are two important parameters in shaping the ultimate amplitudes of the generated ground motions. While the pulsing area percentage primarily governs the amplitudes in the low-frequency range of the simulated accelerograms, stress drop exerts its influence on the amplitudes at higher frequencies. Lower stress drop leads to reduced amplitudes in the response spectra at higher frequencies. As a result, by these two parameters, it becomes possible to generate ground motion time histories with varying amplitudes at both high and low frequencies. However, it is essential to note that this process should not involve random choices; the selected simulation parameters should align with the properties of

the earthquake under study.

The ultimate equation of the stochastic finite fault method introduced by Motazedian and Atkinson [10] is given as follows:

$$A_{ij}(f) = C \cdot H_{ij} \cdot M_{0ij} \frac{(2\pi f)^2}{[1 + (f_{0ij})^2]} \frac{1}{R_{ij}} \exp\left(-\frac{\pi f R_{ij}}{Q(f)\beta}\right) \exp(\pi f \kappa) \cdot A(f) \qquad (2.28)$$

In conclusion, the stochastic finite fault methodology offers an effective and robust technique for generating accurate synthetic data for seismic events. The inclusion of dynamic corner frequencies and other enhancements in the updated EXSIM program enables the simulation to capture the complexity of earthquake behavior and improves the reliability of ground motion predictions for engineering and hazard assessment applications. In this study, the stochastic finite-fault approach was used following the methodology developed by Motazedian and Atkinson [10].

3. STOCHASTIC SIMULATIONS OF THE 2020 ELAZIĞ-SİVRİCE EARTHQUAKE

3.1. General

This chapter undertakes the stochastic finite-fault simulation of the 24 January 2020 Elazığ-Sivrice earthquake in the vicinity of the causative fault. For this objective, the models and data from previous studies suitable for the seismotectonic structure of the region are adopted and critically evaluated to identify a simulation model best fit for the region. In order to validate the regional model parameters, observed records and synthetic records were compared. Furthermore, the ground motion amplitudes obtained from synthetic records are compared with GMMs.

The applications of the stochastic finite fault technique are presented to obtain synthetic data of the mainshock. In section 3.2, essential information about the tectonics and seismicity of the study area, Elazığ, is given. In Section 3.3, the ground motion simulation of the mainshock is presented. Firstly, recorded ground motion data are reported in Subsection 3.3.1. Subsection 3.3.2 introduces the model parameters of the mainshock, while Subsection 3.3.3 presents the comparison of the synthetic records with the observed data. Section 3.3.4 provides a comparison of the simulation results with the recorded data and with estimations from GMMs.

3.2. Background Information

On January 24, 2020, at 20:55 local time (17:55 UTC), a significant earthquake occurred in the Sivrice district of Elazığ province in eastern Türkiye. Also known as the 2020 Elazığ earthquake, the Elazığ-Sivrice earthquake's magnitude, epicenter, and depth were reported by different institutes (Table 3.1 and Figure 3.1).

Table 3.1. Characteristics and location of the mainshock

Reported by	AFAD	KOERI	INGV	GFZ	USGS	EMSC
Magnitude (Mw)	6.8	6.5	6.8	6.8	6.7	6.8
Depth (km)	8.06	5.0	11.0	10.0	11.9	15.0
Longitude	39.06	39.24	39.12	39.20	39.08	39.22
Latitude	38.36	38.37	38.39	38.36	38.39	38.37

The magnitude of the main event was reported as 6.8 by AFAD and as 6.5 by KOERI. The Elazığ-Sivrice earthquake was felt across the Elazığ and Malatya provinces, from Lake Hazar in the east to the city center of Malatya in the west. The earthquake had a considerable impact, resulting in damage to buildings and infrastructure in the affected area. According to official reports, 41 people lost their lives (37 in Elazığ and 4 in Malatya), while 1,466 people were injured due to this event [40].

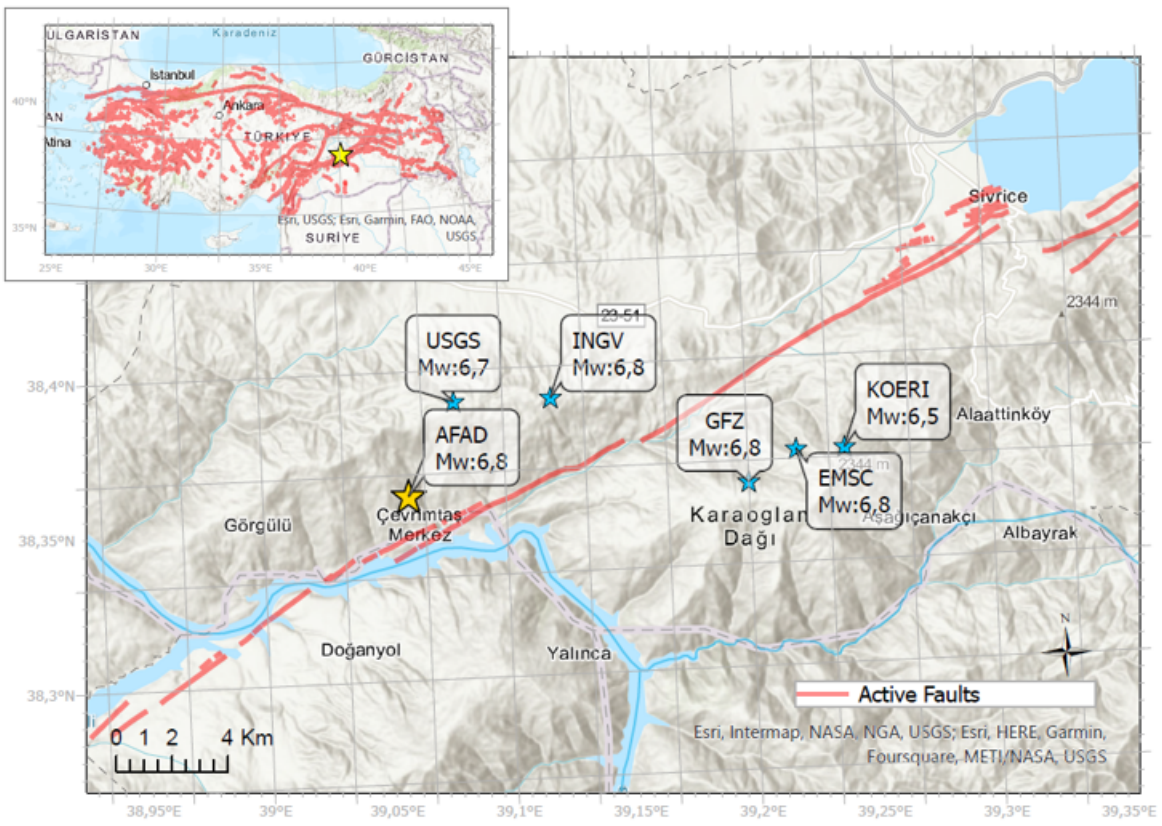

Figure 3.1. Location map of the Elazığ-Sivrice earthquake

Focal mechanism solutions of the mainshock as reported by different seismological institutions are summarized in Table 3.2. The length of the surface rupture created by this left-lateral strike-slip mechanism earthquake was reported as between 20 and 30 km by KOERI and 35-40 km by AFAD. Tatar et al. [41] report a 30 km long surface rupture, and estimate the seismic zone as about 50 km based on the distribution of surface deformation features caused by the Elazığ-Sivrice earthquake seismic sequence.

Table 3.2. Focal mechanism solutions of the mainshock

AFAD	**Strike 1**	**Dip 1**	**Rake 1**	**Strike 2**	**Dip 2**	**Rake 2**
	248	76	1	158	89	166
KOERI	**Strike 1**	**Dip 1**	**Rake 1**	**Strike 2**	**Dip 2**	**Rake 2**
	339	85	176	248	87	-4
USGS	**Strike 1**	**Dip 1**	**Rake 1**	**Strike 2**	**Dip 2**	**Rake 2**
	337	78	-170	245	80	-12

After major earthquakes, hundreds to thousands of aftershocks occur in the same region as the mainshock, which decreases in intensity and frequency over time. After the 2020 Elazığ-Sivrice earthquake, many aftershocks were triggered. 5491 aftershocks occurred in the first year of the mainshock. Their magnitudes were between 0.8 and 5.4. 30 of these aftershocks had magnitudes 4 and larger. The epicenters of the aftershocks were concentrated in the Sivrice and Baskil districts of Elazığ, and in Kale, Pütürge, Doğanyol, and Battalgazi districts of Malatya. The magnitudes of the largest aftershocks were Mw 5.1 (25.01.2020 Elazığ-Sivrice), Mw 4.9 (25.02.2020 Kale-Malatya) and Mw 5.0 (19.03.2020 Elazığ-Sivrice) [42] (Figure 3.2).

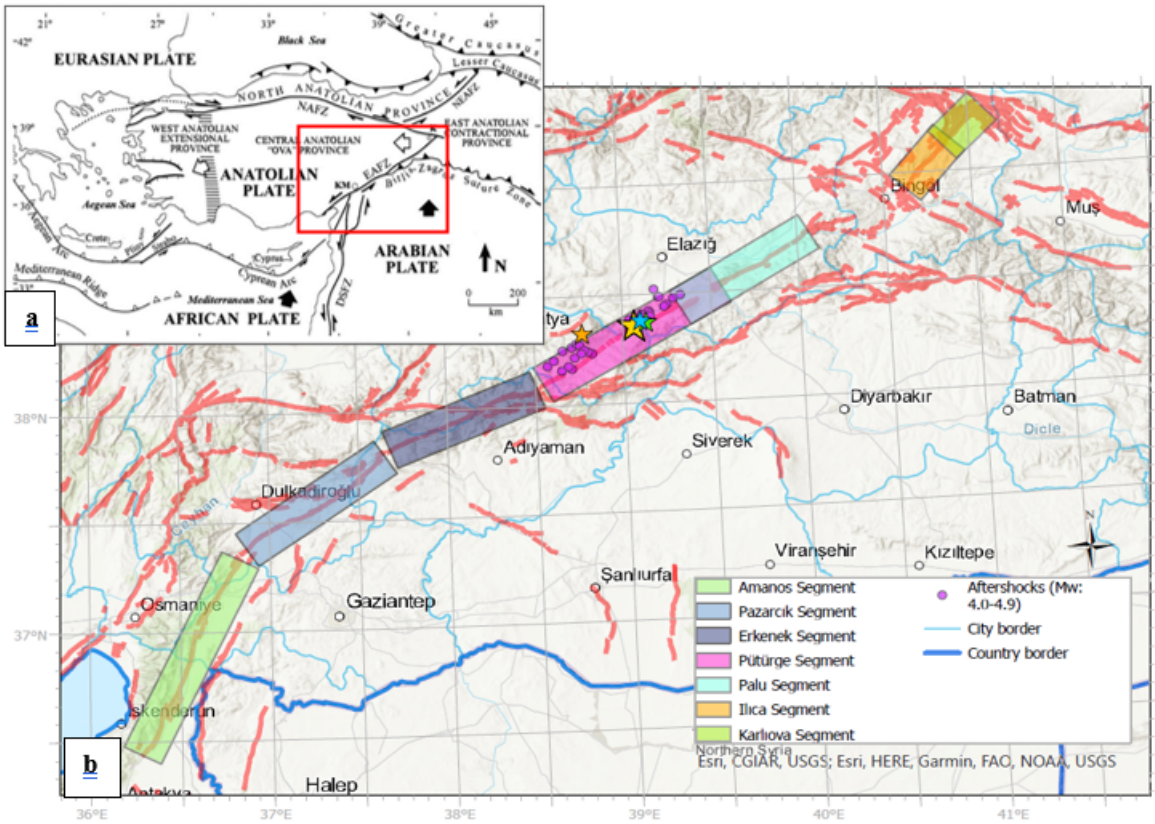

Figure 3.2. a. Tectonic map of Turkey from Bozkurt [43]. b.Segments of the Eastern Anatolian Fault System and location map of the mainshock and aftershocks. The yellow star is the epicenter of the mainshock (Mw 6.8), the green star is the epicenter of the 25.01.2020 Elazığ-Sivrice aftershock (Mw 5.1), the blue star is the epicenter of the 19.03.2020 Elazığ-Sivrice aftershock (Mw 5.0), and the orange star is the epicenter of the 25.02.2020 Kale (Malatya) aftershock (Mw 4.9).

The Elazığ earthquake was associated with the Pütürge segment of the Eastern Anatolian Fault Zone (EAFZ), which had been considered to be a seismic gap that could produce a devastating earthquake in the near future [44].

In order to appropriately evaluate the Elazığ-Sivrice earthquake, the characteristics of the EAFZ on which it is located should be examined. While the East Anatolian Fault (EAF) forms the border between the Arabian block moving to the north and the Anatolian block moving to the west, the other intersections are the North Anatolian Fault (NAF) in Karlıova in the northeast and the Dead Sea Fault (DSF) in the southwest. The NE-SW trending EAF is a left lateral strike-slip fault. EAFZ has an average

width of 30 km and a length of approximately 580 km [44], [40]. According to Duman and Emre [44], EAFZ consists of 7 segments: Karlıova, Ilıca, Palu, Pütürge, Erkenek, Pazarcık and Amanos (Figure 3.2).

Many devastating earthquakes have occurred in and around the seismically active East Anatolian Fault Zone in the historical and instrumental period. In the historical period, major earthquakes with a magnitude of 6.0 and greater in and around the EAFZ, in chronological order; 1513 earthquake (Ms 7.4) in Pazarcik segment [45], 1822 earthquake (Ms 7.5) on Amanos segment [46,47], 1866 earthquake (Ms 7.0) on Karlıova segment, 1874 earthquake (Ms 7.1) on Palu segment 1875 earthquake (Ms 6.7) on Pütürge segment, and the 1893 earthquake (Ms 7.2) on the Ekrenek segment [46]. In the instrumental period, earthquakes of 6.0 and greater occurred in and around the EAFZ, respectively; 1905 Pütürge-Malatya (Ms 6.8) [48], 1908 Malatya (Ms 6.1), 1964 Sincik-Adıyaman (Ms: 6.0), 1966 Varto-Muş (Ms 6.9), 1966 Karlıova-Bingöl (Ms 6.2), 1971 Bingöl (Ms 6.8), 1975 Lice-Diyarbakır (Ms 6.6), 1986 Doğanşehir-Malatya (Mw 6.0), 2003 Pülümür-Tunceli (Mw 6.3) and 2010 Kovancılar-Elazığ (Mw 6.1) earthquakes [40].

The 24.01.2020 Mw 6.8 Elazığ Sivrice earthquake is one of the three largest earthquakes that took place on EAF in the 20th century.

3.3. Ground Motion Simulation of The Mainshock, 24.01.2020 Elazığ-Sivrice earthquake (Mw: 6.8)

3.3.1. Recorded Ground Motion Data of the mainshock

The 24.01.2020 Elazığ-Sivrice earthquake was recorded by 243 strong motion stations. Since far-field ground motions are not of great importance in terms of the damage potential of the event, 27 stations located within 100 km of the fault rupture were selected in this study. All raw acceleration time histories of recorded strong ground motion data used in this study are sourced from the website https://tadas.afad.gov.tr/event-detail/8071. The location of selected strong ground motion stations that recorded the

mainshock is shown in Figure 3.3.

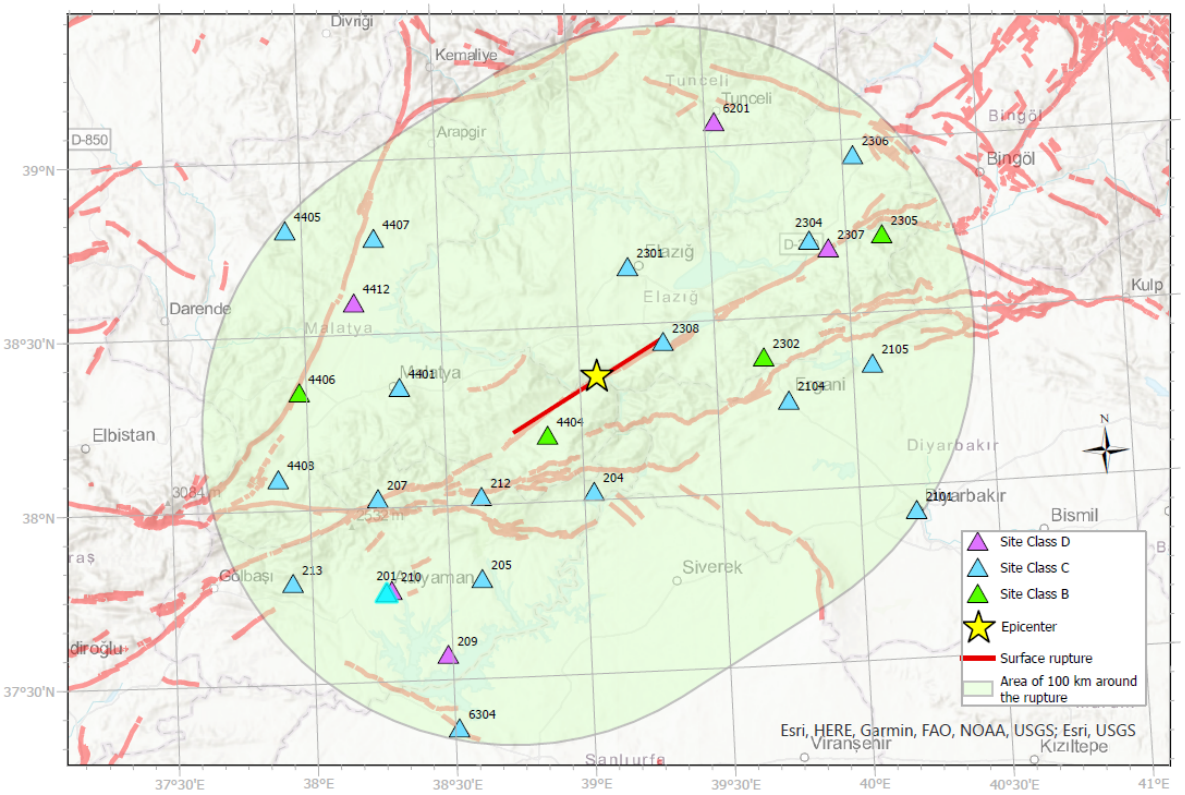

Figure 3.3. Locations of strong ground motion stations in the study area

The raw acceleration time histories were baseline-corrected and filtered using a 4th-order Butterworth filter in a band-pass frequency range of 0.5-25 Hz. The names, codes, coordinates, Vs30 values, and associated site classes based on the National Earthquake Hazard Reduction Program (NEHRP) classification, peak ground accelerations, and epicentral distances of 27 stations used in this study are listed in Table 3.3. For stations without reported Vs30 values, Vs30 values were assigned and classified using regional geological maps (QTM - Quaternary, Tertiary, Mesozoic) provided by MTA (General Directorate of Mineral Research and Exploration).

Table 3.3. Recordings of the 24.01.2020 Elazığ-Sivrice earthquake

Code	**Station**	**Lat** (^{o}**N**)	**Lon** (^{o}**E**)	**Vs30** (cm/s)	**Site Class (Nehrp)**	**Repi** (km)	**Rrup** (km)	**PGA (g) Geomean (EW-NS)**
2308	Sivrice	38,45	39,31	450	C	23,81	0,7	0,256
4404	Pütürge	38,2	38,87	1380	B	24,55	5,77	0,238
212*	Sincik	38,03	38,62	406	C	53,21	22,15	0,044
2301	Merkez	38,67	39,19	407	C	36,39	24,28	0,126
204	Gerger	38,03	39,03	555	C	36,81	27,61	0,111
2302	Maden	38,39	39,68	907	B	53,51	37,66	0,033
205	Kahta	37,79	38,62	660	C	74,25	43,7	0,028
4401*	Merkez	38,35	38,34	481	C	63,04	43,98	0,080
2104*	Ergani	38,26	39,76	406	C	61,64	49,31	0,029
207	Çelikhan	38,03	38,25	660	C	80	53,7	0,033
2304	Kovancılar	38,72	39,86	489	C	80,36	61,94	0,010
210*	Merkez	37,77	38,29	333	D	94,63	64,23	0,021
201	Merkez	37,76	38,27	391	C	96,3	66,05	0,041
6201*	Merkez	39,07	39,53	333	D	89,46	66,21	0,010
2307	Palu	38,7	39,93	329	D	84,35	67,3	0,015
209*	Samsat	37,58	38,48	333	D	100,72	68,5	0,065
4412*	Yazıhan	38,6	38,18	333	D	80,96	69,29	0,018
4407	Arguvan	38,78	38,26	735	C	83,78	75,65	0,027
2105*	Dicle	38,36	40,07	406	C	87,92	77,34	0,012
4406	Akcadağ	38,34	37,97	815	B	95	79,42	0,024
2305	Beyhan	38,73	40,13	907	B	101,52	87,12	0,004
6304	Bozada	37,37	38,51	376	C	120,63	87,5	0,061
4408	Doğanşehir	38,1	37,89	654	C	106,78	87,54	0,014
2306	Karakocan	38,96	40,04	663	C	107,88	89,22	0,005
213*	Tut	37,8	37,93	589	C	117,29	92,2	0,037
2101	Bağlar	37,93	40,2	519	C	110,47	100	0,026
4405	Hekimhan	38,81	37,94	579	C	109,79	100	0,013

* Stations with no previously reported Vs30 values; the Vs30 values at these stations are estimated from QTM maps.

3.3.2. Selection of Model Parameters

To reliably simulate an earthquake input parameters associated with source, path, and site effects must be defined correctly. The simulation parameters adopted in this study are given in Table 3.4 and the slip model is given in Figure 3.4. Details on the selection of input parameters, models, and parameter values are provided subsequently in this section.

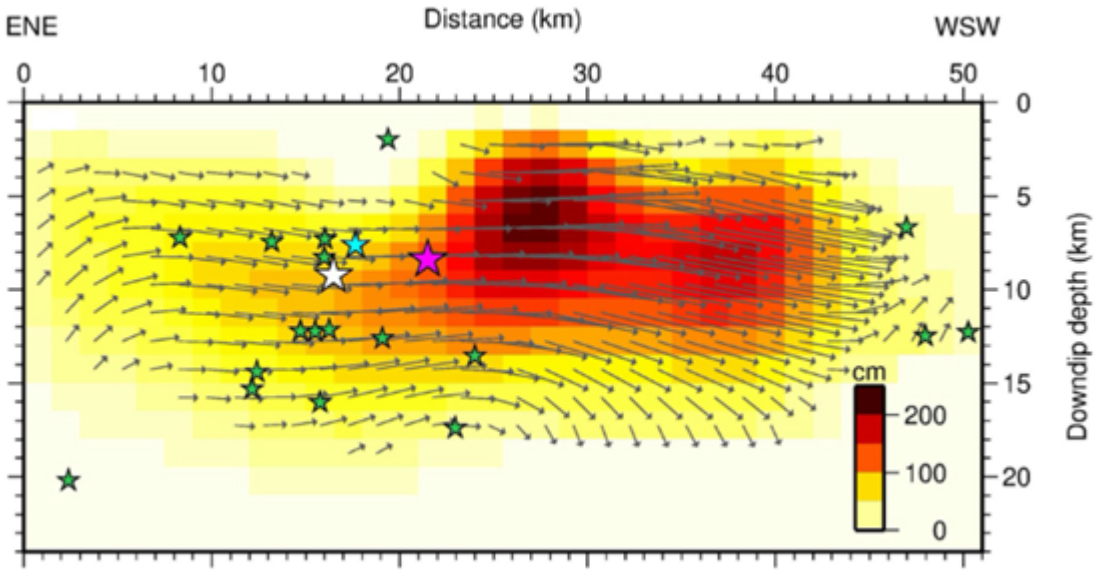

Figure 3.4. Slip distribution proposed by Cheloni and Akinci [49]. The pink and white stars represent the location of the 24 January 2020 Elazığ earthquake provided by AFAD and KOERI, respectively; the blue and green stars are, respectively, the major aftershocks with M> 5 and M> 4 projected on the fault surface (within 3 km).

The validity of input parameters was obtained by comparing the generated ground motions with those observed during the 2020 Elazığ-Sivrice earthquake in both time and frequency domains. The goodness of fit between observed and simulated ground motions is calculated with the help of the model bias equation. The E(f) error function can be defined as :

$$E(f) = \frac{1}{n}\sum_{i=1}^{n} log\left(\frac{A_i(f)_{observed}}{A_i(f)_{simulated}}\right) \tag{3.1}$$

Table 3.4. Input parameter values used in the simulation of the 2020 Elazığ-Sivrice earthquake

Parameter		**Value**		**References**
Source Parameter	Moment Magnitude	6.8		Afad
	Corner on upper edge of fault	38.42364 (^{o}N); 39.46586 (^{o}E)		Cheloni and Akinci [49]
	Depth of Corner on Upper Edge of Fault	0		Cheloni and Akinci [49]
	Fault Type	SS		Afad
	Strike; Dip	248; 76		Afad
	Fault Length; Fault Width	51 Km; 24 Km		Cheloni and Akinci [49]
	Subfault Length; Subfault Width	1.5 Km; 1.5 Km		Cheloni and Akinci [49]
	Slip Distribution			Cheloni and Akinci [49]
	Number of subfaults	34x16=544 subfaults		Cheloni and Akinci [49]
	Location of hypocenter within subfaults	22; 8		Cheloni and Akinci [49]
	Rupture Velocity	0.8 Beta		
	Stress Drop	7 Mpa/ 70 Bar		This study
	Pulsing Area Percentage	50 Percent		Boore [17]
	Window Function	Saragoni-Hart		Boore [7]
Path Parameter	Geometrical Spreading	$r^{-1.0}$ $r \leq 60km$		This study
		$r^{-0.5}$ $r > 60km$		
	Anelastic Attenuation (Quality Factor)	Q(f)= $180f^{0.45}$		Cheloni and Akinci [49]
	Path Duration Model	Rrup (km)	Dp (s)	Boore and Thompson [50]
		0	0	
		7	2.4	
		45	8.4	
		125	10.9	
		175	17.4	
		270	34.2	
		Slope of last segment	0.156	
	Crustal Density	2800 kg/m3		
	Crustal Shear-Wave Velocity (Beta)	3.5 kms-1		Gök et al. [51]
Site Parameter	Site Amplification	NEHRP sites		Boore and Joyner [30]
	Crustral Amplification	-		
	Kappa Factor	0.035-0.04 s		Boore and Joyner [30]

In the equation, n indicates the number of modeled stations, while A_i represents the Fourier amplitudes of acceleration time histories in the i^{th} station over the frequency range of interest for both recorded and simulated ground motions. The error function can be calculated as a measure of model performance for a single station or for all stations used. In this section model bias is used to assess the effect of selecting different parameter values on simulated waveforms. How and why model parameters and parameter values are chosen is also discussed. The frequency range for model bias estimations is 0.5Hz-25Hz.

Residual analysis of peak ground accelerations (PGA) and peak ground velocities (PGV) was carried out in order to estimate the overall range that they vary and utilized as a measure of improvement between different models. They are also used to check if there is a systematic bias in the results with respect to fault distance and site class. Station-based PGA and PGV residuals are defined as:

$$Residual_{PGA} = log10\left(\frac{PGA_{observed}}{PGA_{simulated}}\right) \tag{3.2}$$

$$Residual_{PGV} = log10\left(\frac{PGV_{observed}}{PGV_{simulated}}\right) \tag{3.3}$$

In all comparisons with respect to the observed data, the geometric mean of the two horizontal components is used.

The essential source parameters are seismic moment, fault geometry, rupture velocity, slip distribution, stress drop, and pulsing area percentage. In order to determine the optimum model parameter values, simulations were carried out with different slip models, stress drop values, and pulsing area percentages. The influence of selected parameter values was traced by changing a single parameter while keeping all other parameters constant. The analysis was continued by selecting the parameters that provide the best match between the observed and synthetic records in both time and frequency domains.

In this study, firstly we evaluated the slip distribution model. First, the random slip distribution model generated by EXSIM, which provides the moment magnitude of the event through the conservation of the seismic moment, is used. Secondly, the slip model proposed by Cheloni and Akinci [49] for the 24 January 2020 Elazığ earthquake was used. The rectangular left-lateral strike-slip fault plane, which is 50 km long and 25 km wide, is divided into 34 sub-faults along the strike and 16 sub-faults along the dip directions. The dimension of each sub-fault is 1.5 km x 1.5 km. The slip distribution shown in Figure 3.4 has been converted to slip weights and used as such in EXSIM.

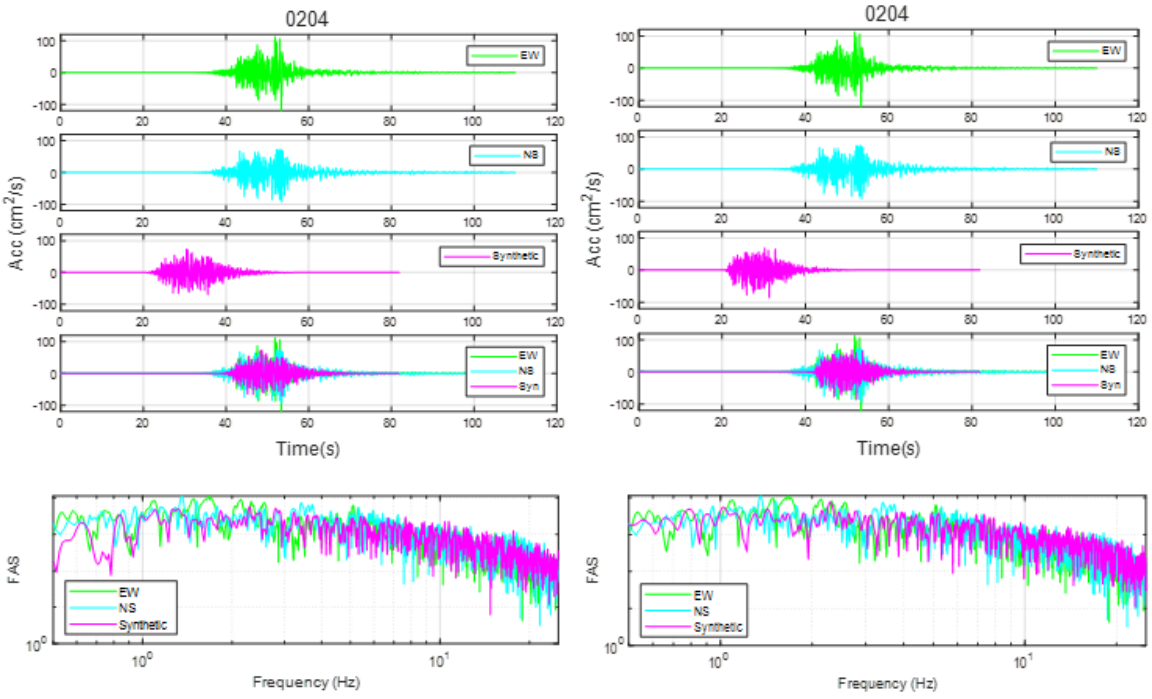

(a) (b)

Figure 3.5. Comparison of accelerations and FAS for different slip models at station 0204 ((a) random slip (b) slip model proposed by Cheloni and Akinci [49])

In order to show the effect of different models, station 0204, one of the stations close to the fault rupture, was representatively selected (Figure 3.5). The comparison is carried out uniformly for all stations in the dataset. The presentation of results at a single station in this subsection is for the sake of simplicity. The observed peak ground acceleration (PGA) at station 0204 is 109.32 cm/s^2. While the PGA of the synthetic record obtained with the random slip model is 87.57 cm/s^2, the PGA value of the synthetic record obtained with the Cheloni and Akinci [49] slip model is 103.61 cm/s^2.

The fit between the Fourier Amplitude Spectra (FAS) of synthetic and simulated data is satisfactory for both slip models, with the Cheloni and Akinci [49] model being slightly superior to the random slip model.

To present an overall picture of the effect of our model selection at all stations, residuals between observed and simulated PGAs and peak ground velocities (PGV) are estimated (Figures 3.6 and 3.7). The residuals are plotted against rupture distance and grouped in terms of site classes in order to observe if there is a systematic bias in our simulation model with respect to fault distance and site class. It is evident from the figures that there is no distance and site class bias in the model. However, the adoption of the Cheloni and Akinci [49] slip model provided PGA biases (Figure 3.6) distributed over a narrower range as compared to the random slip model. The PGV biases associated with the random slip model (Figure 3.7) tend to be slightly on the negative side, indicating that the simulations are larger than observations for the majority of stations. The situation improved when Cheloni and Akinci [49] slip model was used represented by a more uniform distribution of negative and positive biases. It is observed though that the general range of biases is slightly wider as compared to the random slip model.

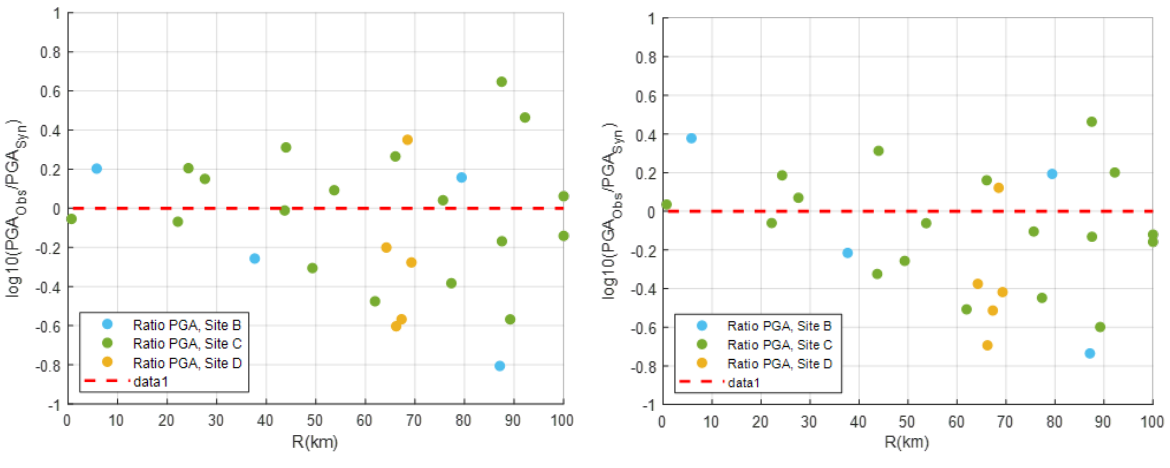

(a) (b)

Figure 3.6. Effect of slip distribution models on PGA residuals. Station-specific residuals versus rupture distance for (a) random slip and (b) slip model proposed by [49]. A color code is used to mark stations of different site classes.

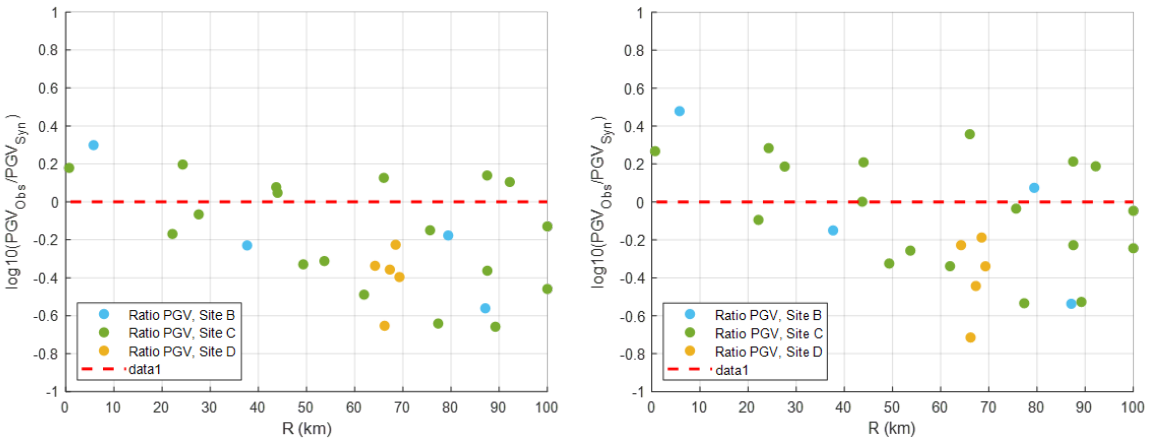

(a) (b)

Figure 3.7. Effect of slip distribution models on PGV residuals. Station-specific residuals versus rupture distance for (a) random slip and (b) slip model proposed by Cheloni and Akinci [49]. A color code is used to mark stations of different site classes.

Figure 3.8b presents the model bias over the frequency range of interest when the Cheloni and Akinci [49] slip model is used in the simulation. Figure 3.8a summarizes the results of simulations carried out to develop an understanding of the effects stress drop variations have on the synthetics. Stress drop bears the largest uncertainty among the source parameters. One reason for this is that the stress drop exhibits a quite large range of variability making the development of models less reliable. Known to affect particularly the PGAs, it is often used as a leverage to improve and refine the simulations using stochastic approaches, when other parameters are decided for. It is important to develop an understanding of the stress drop levels that are fit for the simulation exercise in question and their effects on the synthetics. Model biases are plotted for stress drops of 50, 70, and 90 bars using a random slip model in Figure 3.8a. More information on the particulars of the three models can be found in Table 3.5.

Figure 3.8a suggests that with the increase of stress drop values the average synthetic Fourier amplitudes also increase. A stress drop of 70 bars is estimated to be a general optimum with average synthetic Fourier amplitude misfits (+ or -) remaining between +0.5/-0.5 and distributed more or less evenly over the considered frequency

range. Figure 3.8b shows that the performance of the model increases when a non-random slip model is used, constraining the model bias function between about +0.3/-0.3.

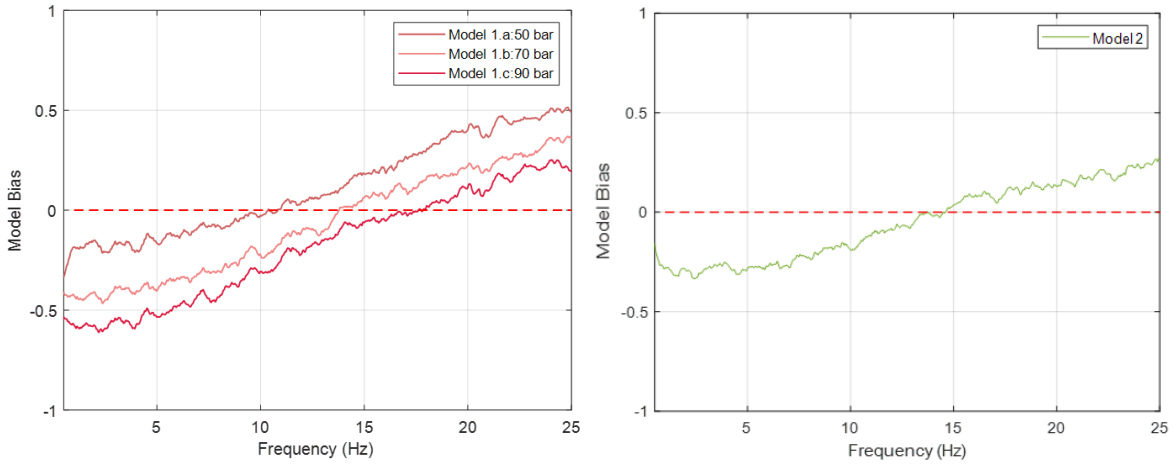

(a) (b)

Figure 3.8. Error functions averaged over stations in the data set, when different stress drop values and random slip model are used, and (b) when a stress drop of 70 bars and the Cheloni and Akinci [49] slip model is used. Other parameter values used are indicated in Tables 3.4 and 3.5.

Overall, when the Cheloni and Akinci [49] slip model is used together with a stress drop of 70 bars it was observed that station-specific synthetics were generally better. Based on these elaborations we selected the slip model by Cheloni and Akinci [49], and moved on to other parameters in search of an optimum simulation model for the Elazığ-Sivrice earthquake.

The effect of geometrical spreading functions, Q models (quality factor), and duration models were studied next.

We have examined three different frequency-dependent geometric spreading models. The starting model was the geometric spreading function of Akinci and Anto-

nioli [15](Equation 3.4).

$$\begin{array}{ll} r^{-1.0} & r \leq 100km \\ r^{-0.5} & r > 100km \end{array} \tag{3.4}$$

The second model was modified from the model presented in Equation 3.4. It can be seen as in Equation 3.5. The rationale behind this modification will be discussed in the coming paragraphs.

$$\begin{array}{ll} r^{-1.0} & r \leq 60km \\ r^{-0.5} & r > 60km \end{array} \tag{3.5}$$

The third geometric spreading model was proposed by Akinci et al. [52] and is expressed as in Equation 3.6.

$$\begin{array}{ll} r^{-1.0} & r \leq 25km \\ r^{-0.5} & r > 25km \end{array} \tag{3.6}$$

Synthetics were generated using these three models, other parameters being the same. PGA and PGV residuals plotted with respect to fault distance and grouped in terms of their site classes are shown in Figure 3.9 and 3.10 respectively.

Figure 3.9a shows residual PGAs for the Akinci and Antonioli [15] model, with the r parameter set at 100 km. The figure shows at stations with fault rupture distances larger than about 60 km the spread of the PGA residuals is much wider than at distances less than 60 km. Until about 60 km rupture distance, the residuals remain within the +0.4/-0.4 range, while after 60 km they are distributed between +0.5/-0.7. Therefore it was decided to modify the geometric spreading model as presented in Equation 3.4 by setting the distance where the power changes from -1.0 to -0.5 at 60

km. In other words the spectral amplitudes in the adopted model decay as 1/R at distances less than 60 km, beyond 60 km the geometric spread is defined as $R^{-0.5}$.

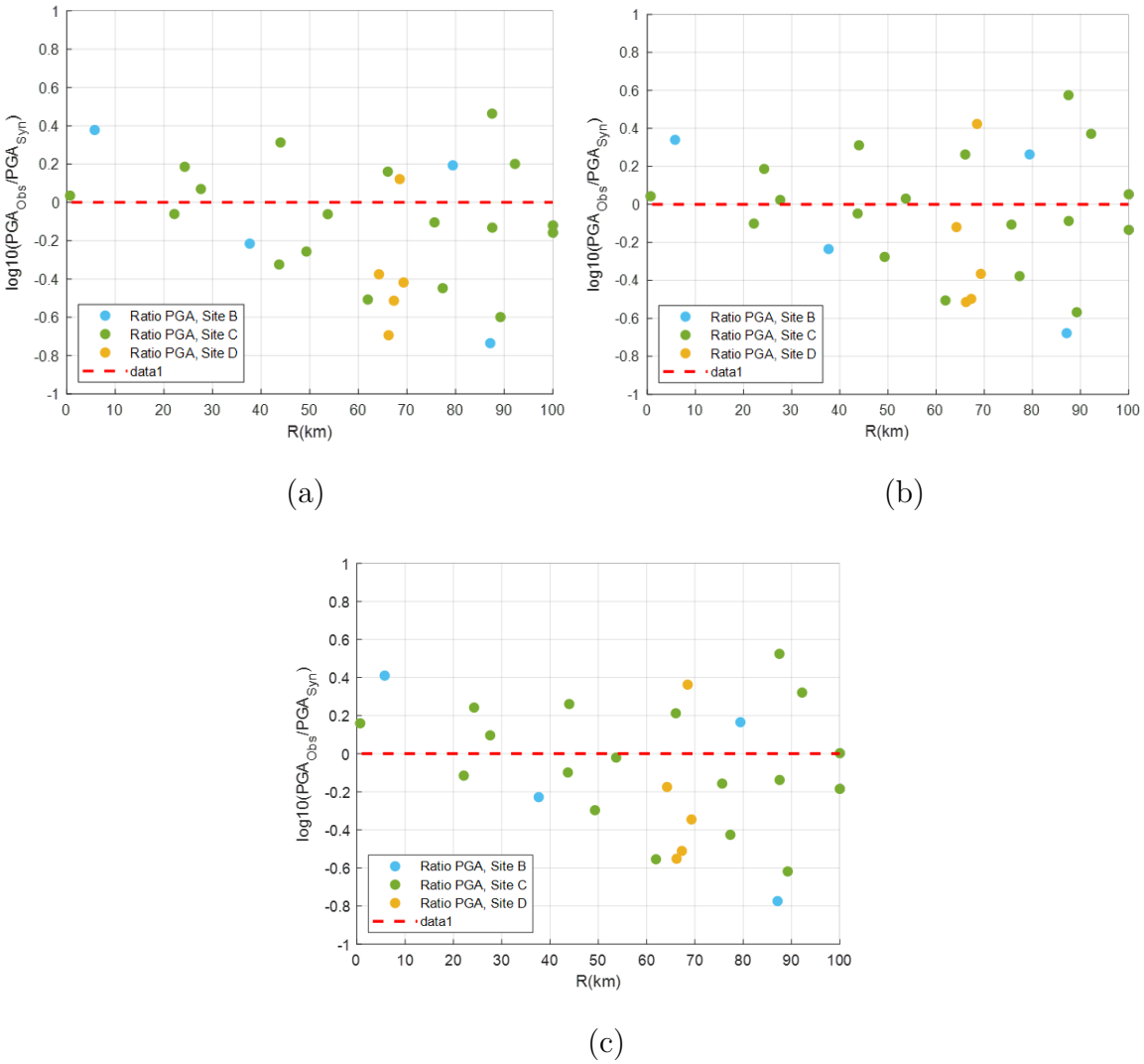

(a) (b)

(c)

Figure 3.9. Effect of geometrical spreading models on PGA residuals (a)$r^{-1.0}$ $r \leq 100km$, $r^{-0.5}$ $r > 100km$ by Akinci and Antonioli [15] (b) $r^{-1.0}$ $r \leq 60km$, $r^{-0.5}$ $r > 60km$ (c) $r^{-1.0}$ $r \leq 25km$, $r^{-0.5}$ $r > 25km$ by Akinci et al. [52]

When Figures 3.9 and 3.10 are examined it can be seen that the model performing relatively poorly is Akinci et al [52]. Although there was only a slight improvement in the distribution of PGA residuals when the modified spreading model was used, still it was the best model as can be seen in the model bias plots across three different models.

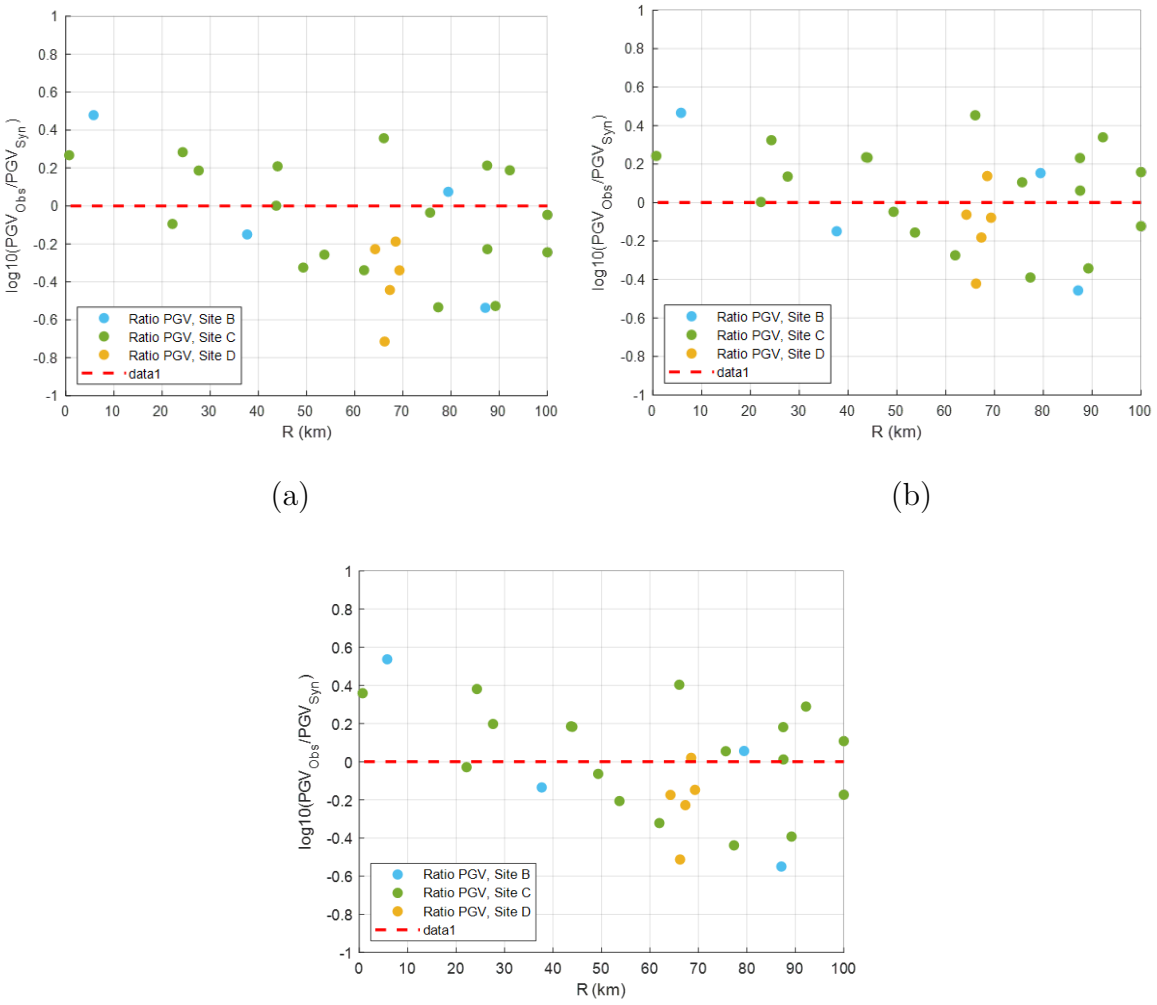

(a) (b)

(c)

Figure 3.10. Effect of geometrical spreading models on PGV residuals (a)$r^{-1.0}$ $r \leq 100km$, $r^{-0.5}$ $r > 100km$ by Akinci and Antonioli [15] (b) $r^{-1.0}$ $r \leq 60km$, $r^{-0.5}$ $r > 60km$ (c) $r^{-1.0}$ $r \leq 25km$, $r^{-0.5}$ $r > 25km$ by Akinci et al. [52]

Figure 3.11 shows the average modal biases considering all stations obtained using three different geometrical spreading models. The figure indicates that the model proposed in this study performs best in our frequency range of interest.

For this reason, the geometrical spreading model defined for this study was chosen as the preferred model.

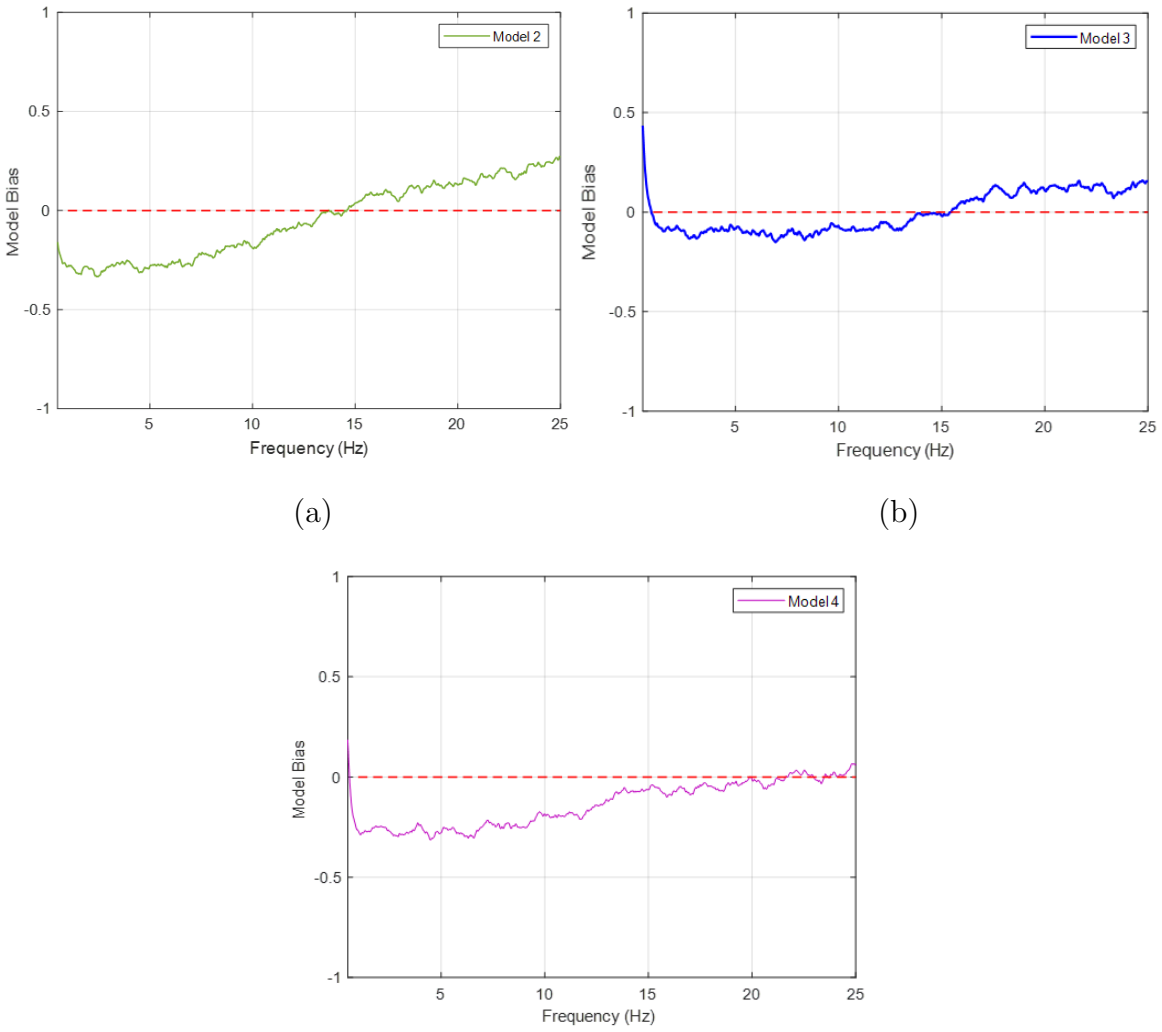

Figure 3.11. Effect of geometrical spreading models. Averaged model biases obtained from the error functions of 27 stations in the frequency domain (a) Akinci and Antonioli [15] (b) this study (c) Akinci et al. [52])

The model comparison was made for two different frequency-dependent quality functions. Results are given in Figures 3.12, 3.13 and 3.14. The model presented by Akinci et al. [53] as $Q(f) = 100f^{0.43}$, resulted in an overestimation of FAS levels for frequencies up to 5–6 Hz. This situation was observed at almost all stations.

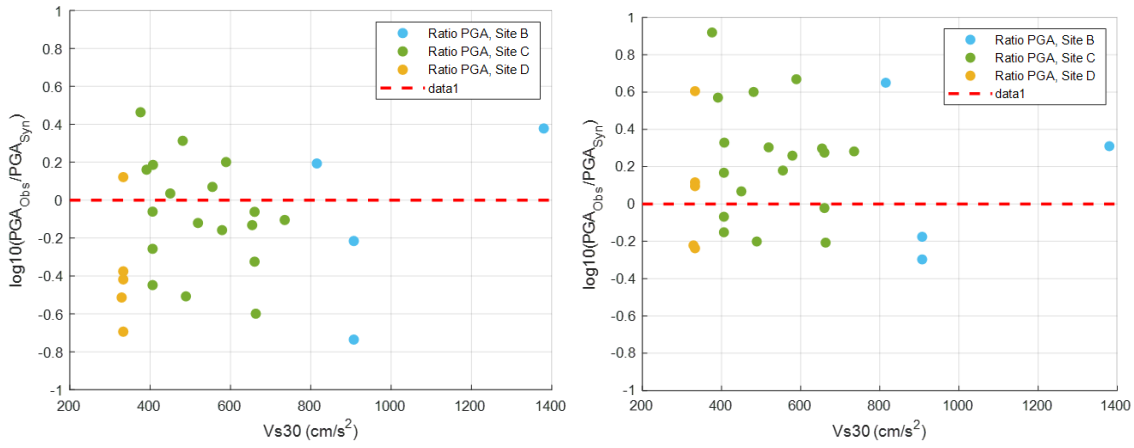

(a) (b)

Figure 3.12. Effect of different Q models on PGA residuals vs Vs30. (a) Akinci et al. [54] $Q(f) = 180f^{0.45}$ (b) Akinci et al. [53] $Q(f) = 100f^{0.43}$

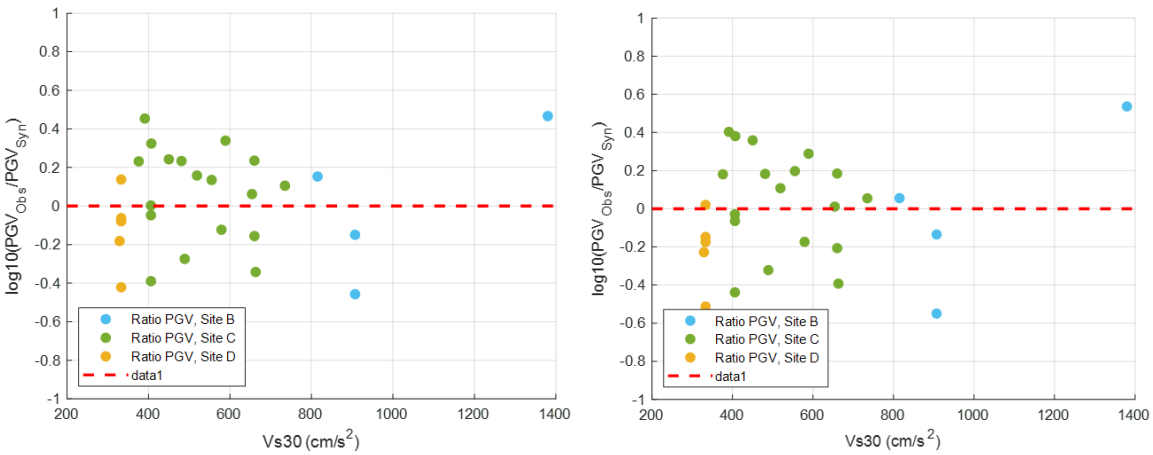

(a) (b)

Figure 3.13. Effect of different Q models on PGV residuals vs Vs30. (a) Akinci et al. [54] $Q(f) = 180f^{0.45}$ (b) Akinci et al. [53] $Q(f) = 100f^{0.43}$

When the results of the model presented by Akinci et al. [54] with $Q(f) = 180f^{0.45}$ were examined, it was determined that the observed and simulated values in all frequency ranges were close to each other. The residual analysis of recorded and synthetic PGAs and PGVs yielded a similar conclusion as well.

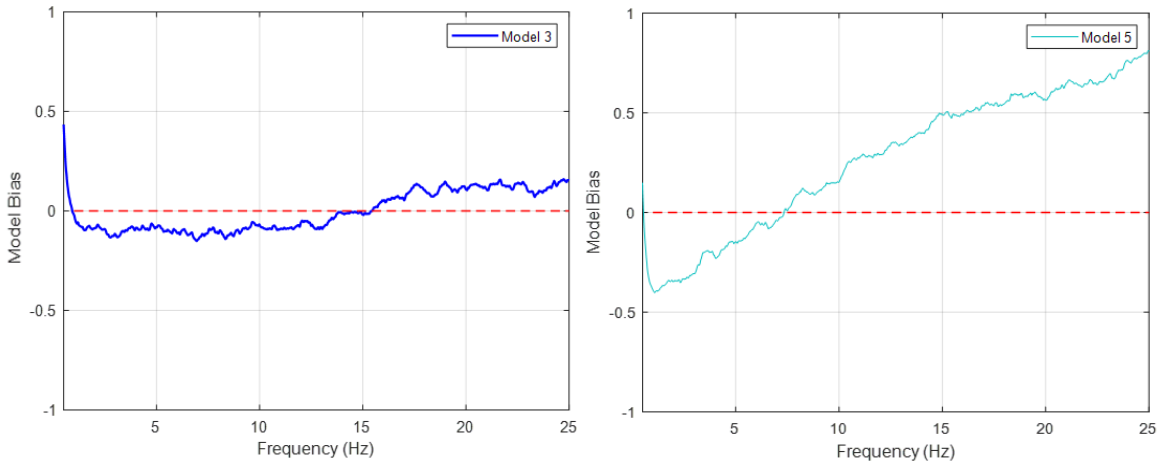

(a) (b)

Figure 3.14. Effect of Q models on all stations. Averaged model biases obtained from the error functions of 27 stations in the frequency domain (a) Akinci et al. [54] $Q(f) = 180f^{0.45}$ (b) Akinci et al. [53] $Q(f) = 100f^{0.43}$

After selecting the geometric spreading and the Q models, the only remaining model to be decided was the duration model. Two different models were compared in order to choose the most appropriate duration model. A model with a distance-dependent form defined as T = T0 + 0.1R by [55], which is also used in the Cheloni and Akinci [49] study, was tested. In the results from this model, synthetic acceleration records did not match well with observed acceleration records. For this reason, the model proposed by Boore and Thompson [50] was used as the path duration model in order to provide a better match with the records and to obtain a longer S wave duration.

Figure 3.15 shows the effect of two duration models on the synthetic accelerations at station 0204. It can be observed that Boore and Thompson [50] perform better in time and frequency domains. The distribution of PGA and PGV residuals are shown for the two duration models against fault distance and colored for different site classes are shown in Figure 3.16 and Figure 3.17 respectively.

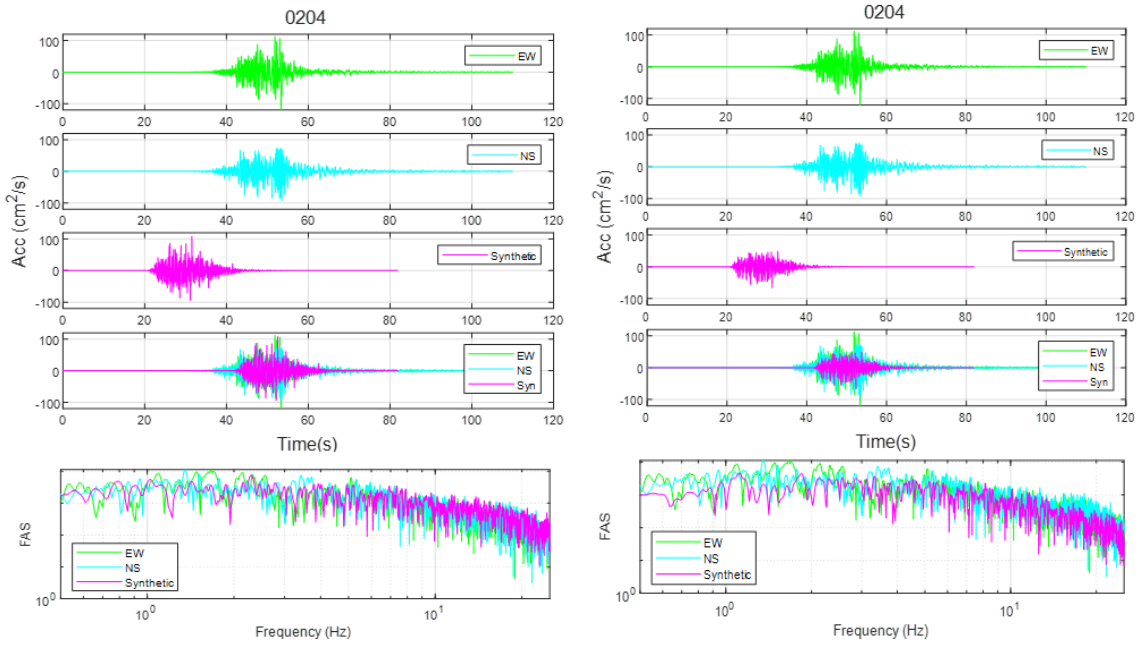

(a) (b)

Figure 3.15. Comparison of different duration models at station 0204 (a) Boore and Thompson [50] duration model (b) Atkinson and Boore [55] model

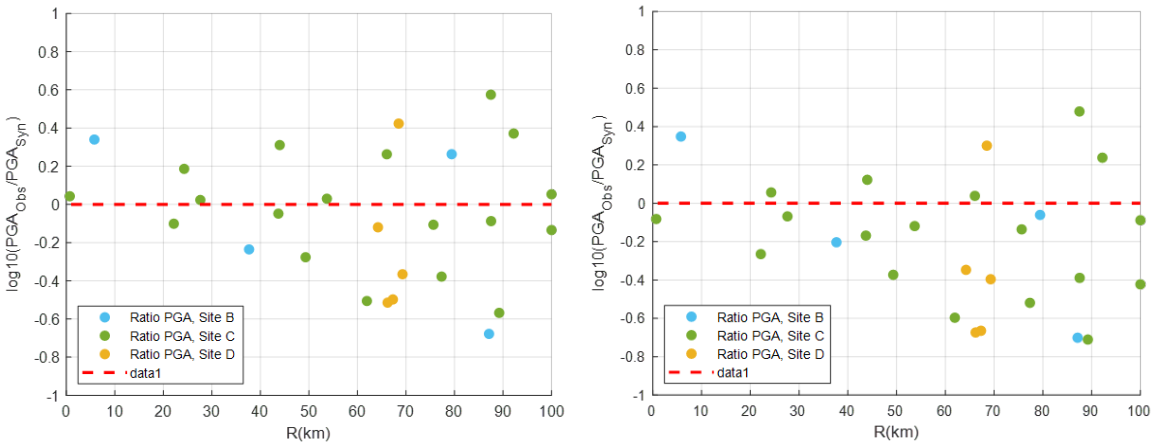

(a) (b)

Figure 3.16. Effect of different duration models on PGA residuals. (a) Boore and Thompson [50] duration model (b) Atkinson and Boore [55] model

In Figure 3.18 model misfits estimated when two duration models are used are shown in the frequency range of interest. It is evident from the figures that the Boore and Thompson [50] model performs generally better.

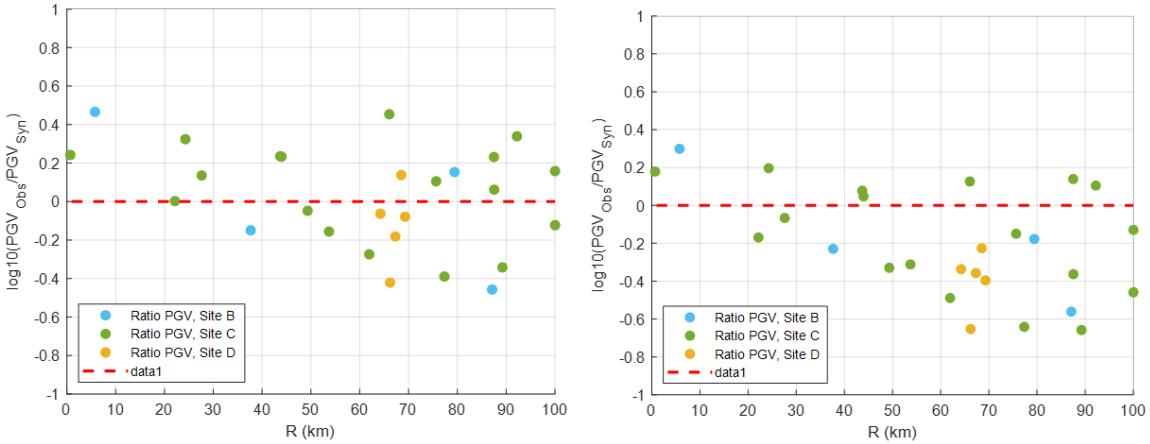

(a) (b)

Figure 3.17. Effect of different duration models on PGV residuals. (a) Boore and Thompson [50] duration model (b) Atkinson and Boore [55] model

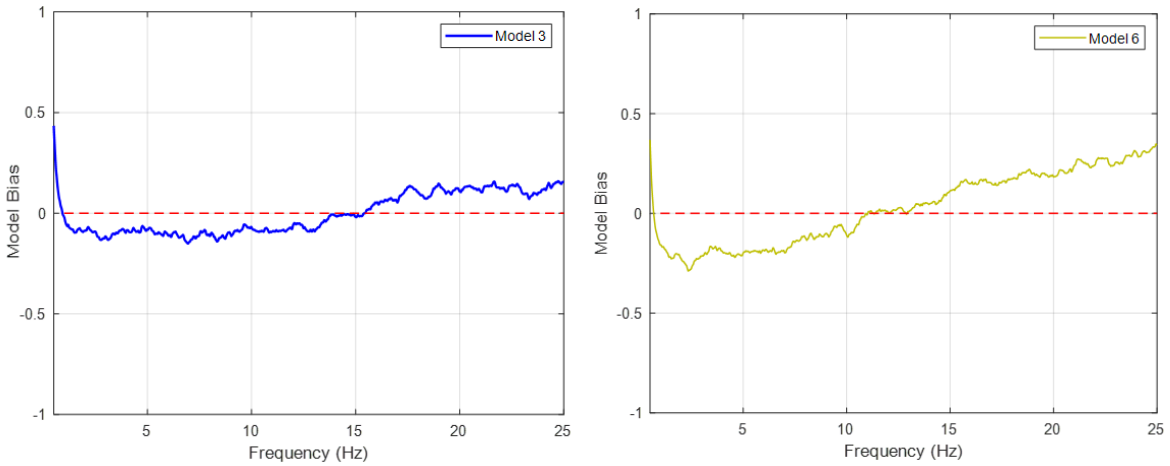

(a) (b)

Figure 3.18. Effect of duration models. Averaged model biases obtained from the error functions of 27 stations in the frequency domain (a) Boore and Thompson [50] duration model (b) Atkinson and Boore [55] model

After identifying the Boore and Thompson [50] model as the preferred duration model, the site amplification models were checked. Two different models were compared to choose the most suitable site amplification factors for our study area. Firstly, we used the amplification factors of Margaris and Boore [56] corresponding to NEHRP site classes D, C, and B for stations with Vs30 values of 180-360 m/s, 360-760 m/s,

and 760-1500 m/s respectively. Secondly, we used Boore and Joyner's [30] amplification factors. For class B stations, we assigned amplification factors corresponding to generic rock. Results are given in Figures 3.19, 3.20, and 3.21.

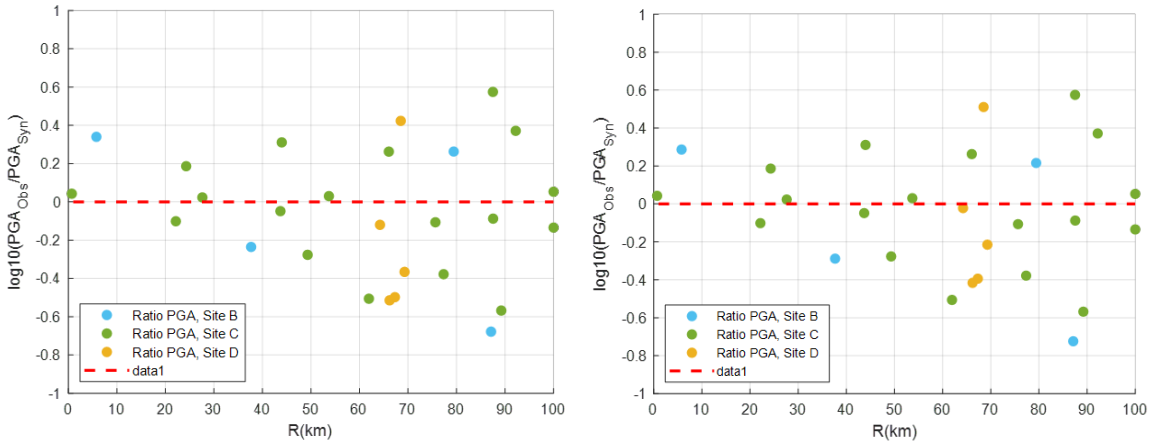

(a) (b)

Figure 3.19. Effect of site amplification models on the distribution of PGA residuals. (a) Margaris and Boore [56] (b)Boore and Joyner [30]

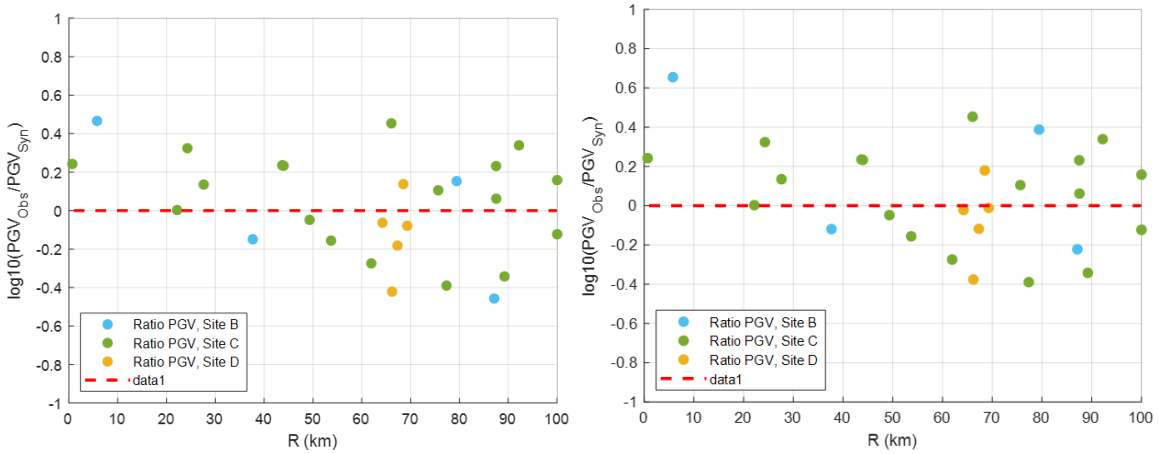

(a) (b)

Figure 3.20. Effect of site amplification models on the distribution of PGV residuals. (a) Margaris and Boore [56] (b)Boore and Joyner [30]

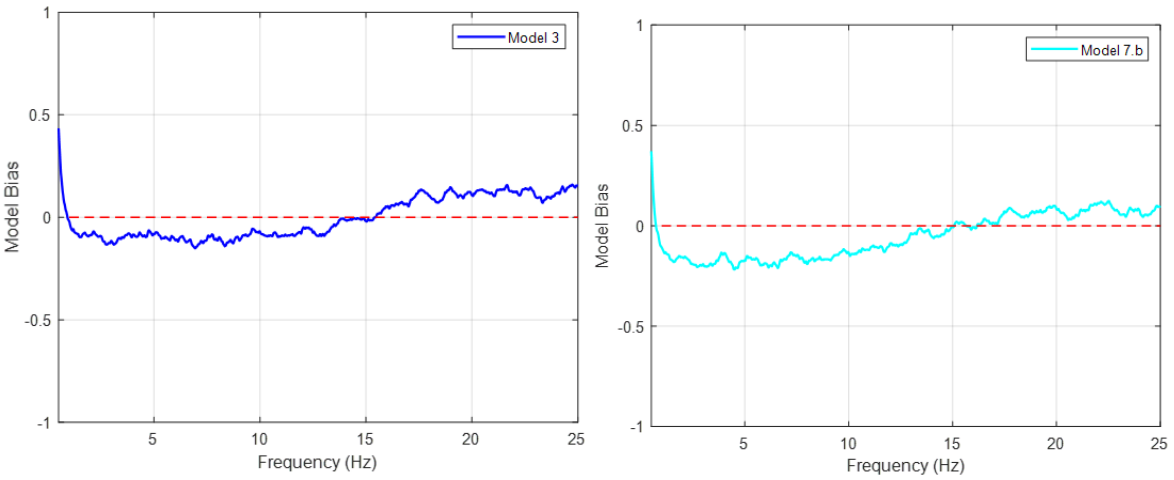

(a) (b)

Figure 3.21. Effect of site amplification models. Averaged model misfits obtained from the error functions of 27 stations in the frequency domain (a) Margaris and Boore [56] (b)Boore and Joyner [30]

The performance of the two models is not too far away from each other. It has been observed that Boore and Joyner's [30] amplification values give better results in the 15-25 Hz frequency range and slightly better distribution of PGA and PGV residuals. Therefore, the Boore and Joyner [30] model was used for site amplification coefficients. For high-frequency decay (k), the following kappa values are adopted as suggested by Boore and Joyner [30]: 0.04 for B-type soils, and 0.035 for C and D-type soils.

As the final step the effect of stress drop was once more examined for the values of 50, 70, 90, and 110 bars, keeping all other parameter values constant. Results presented in Figure 3.22 demonstrate how the choice of the stress drop parameter affects the misfit. Among the four different stress drop values, 70 bar is the one that gives the best results.

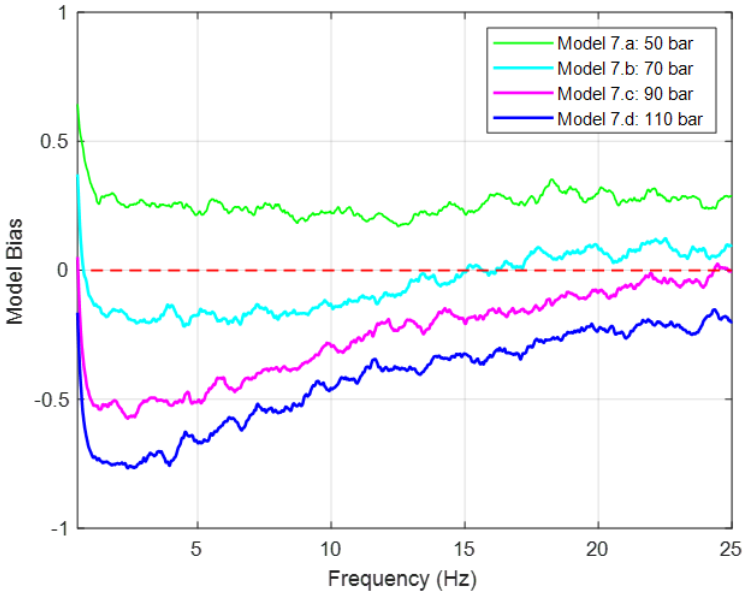

Figure 3.22. Effect of different stress drop parameters.

To provide a basis for comparing the general performance of all models used in the simulation and to track the improvement the root mean square error (RMSE) was utilized. The simulation models tested in this study are summarized and coded in Table 3.5. The remaining parameters are as in Table 3.4.

Table 3.5. Simulation models and their parameters

Simulation Model	**Slip Model**	**Geometrical Spreading**	**Quality Factor**	**Duration Model**	**Stress Drop**	**Site Amplification**
Model 1.a	Random	$r^{-1.0}\ r \leq 100km$ $r^{-0.5}\ r \leq 100km$	$Q(f) = 180f^{0.45}$	Boore and Thompson [50]	50 bar	NEHRP site classes D, C, and B Margaris and Boore [56]
Model 1.b	Random	$r^{-1.0}\ r \leq 100km$ $r^{-0.5}\ r \leq 100km$	$Q(f) = 180f^{0.45}$	Boore and Thompson [50]	70 bar	NEHRP site classes D, C, and B Margaris and Boore [56]
Model 1.c	Random	$r^{-1.0}\ r \leq 100km$ $r^{-0.5}\ r \leq 100km$	$Q(f) = 180f^{0.45}$	Boore and Thompson [50]	90 bar	NEHRP site classes D, C, and B Margaris and Boore [56]
Model 2	Cheloni and Akinci [49]	$r^{-1.0}\ r \leq 100km$ $r^{-0.5}\ r \leq 100km$	$Q(f) = 180f^{0.45}$	Boore and Thompson [50]	70 bar	NEHRP site classes D, C, and B Margaris and Boore [56]
Model 3	Cheloni and Akinci [49]	$r^{-1.0}\ r \leq 60km$ $r^{-0.5}\ r > 60km$	$Q(f) = 180f^{0.45}$	Boore and Thompson [50]	70 bar	NEHRP site classes D, C, and B Margaris and Boore [56]
Model 4	Cheloni and Akinci [49]	$r^{-1.0}\ r \leq 25km$ $r^{-0.5}\ r > 25km$	$Q(f) = 180f^{0.45}$	Boore and Thompson [50]	70 bar	NEHRP site classes D, C, and B Margaris and Boore [56]

Table 3.5. Simulation models and their parameters (cont.)

Simulation Model	**Slip Model**	**Geometrical Spreading**	**Quality Factor**	**Duration Model**	**Stress Drop**	**Site Amplification**
Model 5	Cheloni and Akinci [49]	$r^{-1.0}\ r \leq 60km$ $r^{-0.5}\ r > 60km$	$Q(f) = 100f^{0.43}$	Boore and Thompson [50]	70 bar	NEHRP site classes D, C, and B Margaris and Boore [56]
Model 6	Cheloni and Akinci [49]	$r^{-1.0}\ r \leq 60km$ $r^{-0.5}\ r > 60km$	$Q(f) = 180f^{0.45}$	Atkinson and Boore (1995)	70 bar	NEHRP site classes D, C, and B Margaris and Boore [56]
Model 7.a	Cheloni and Akinci [49]	$r^{-1.0}\ r \leq 60km$ $r^{-0.5}\ r > 60km$	$Q(f) = 180f^{0.45}$	Boore and Thompson [50]	50 bar	NEHRP site classes C, D and GR Boore and Joyner [30]
Model 7.b	Cheloni and Akinci [49]	$r^{-1.0}\ r \leq 60km$ $r^{-0.5}\ r > 60km$	$Q(f) = 180f^{0.45}$	Boore and Thompson [50]	70 bar	NEHRP site classes C, D and GR Boore and Joyner [30]
Model 7.c	Cheloni and Akinci [49]	$r^{-1.0}\ r \leq 60km$ $r^{-0.5}\ r > 60km$	$Q(f) = 180f^{0.45}$	Boore and Thompson [50]	90 bar	NEHRP site classes C, D and GR Boore and Joyner [30]
Model 7.d	Cheloni and Akinci [49]	$r^{-1.0}\ r \leq 60km$ $r^{-0.5}\ r > 60km$	$Q(f) = 180f^{0.45}$	Boore and Thompson [50]	110 bar	NEHRP site classes C, D and GR Boore and Joyner [30]

The RMSE function can be defined as:

$$RMSE_{PGA} = \sqrt{\frac{1}{n}\sum_{i=1}^{n}(PGA_{i,\text{obs}} - PGA_{i,\text{syn}})^2} \tag{3.7}$$

In the equation, n indicates the number of modeled stations, while PGA_i represents the station PGA at the i^{th} station for both recorded and simulated ground motions. This equation, which measures the mean square error between the predicted values and the actual value, was also used for PGVs.

In our simulations, we modified one parameter at a time and tested its effect by comparing the RMSE. We repeated this process for each simulation model to determine the model with minimum RMSE. The results for all simulation models presented above are summarized in Table 3.6. Model 7.b yields the lowest RMSE both for PGA and PGV.

Table 3.6. RMSEs for simulation models

Simulation Model	**RMSE PGA**(cm^2/s)	**RMSE PGV**(cm/s)
Model 1.a	38.8452	5.5246
Model 1.b	36.7811	5.3151
Model 1.c	38.4863	5.4634
Model 2	34.6282	5.2909
Model 3	32.8282	4.9908
Model 4	38.5679	5.4921
Model 5	34.9797	5.4134
Model 6	33.7180	5.3326
Model 7.a	38.7242	5.4108
Model 7.b	**30.6554**	**4.9049**
Model 7.c	36.6830	5.3206
Model 7.d	38.3617	5.4315

3.3.3. Results of Simulations and Discussions

24 January 2020 Elazığ-Silivri earthquake was simulated with EXSIM using the input parameters in Table 3.4. The preferred simulation model is Model 7.b (Table 3.5). The simulation was made for 27 stations within the study area. The raw acceleration time histories were baseline corrected and filtered with a 4th-order Butterworth filter in the band-pass frequency range of 0.5-25 Hz.

Acceleration time histories and the FAS are calculated to compare observed and synthetic waveforms in terms of amplitude, duration, and frequency content. Findings of the 9 stations closest to the fault among 27 stations are examined below (Figures 3.23, 3.24 and 3.25). In these figures, the green curves represent the EW component of the ground motion, the blue curves represent the NS component. The magenta curves are simulated accelerations. The complete set of 27 stations is included in Appendix A.

A comparison of simulated ground motions of 3 stations closest to the surface rupture with observed records is given in Figure 3.23. When station 2308 is evaluated in the time domain, the match between the synthetic and observed records was reasonably well in duration and amplitude. In the frequency domain, at 5 Hz and above, simulated records are slightly higher than observed. Synthetic ground motions obtained for station 4404 matched the observed ground motion in duration, but an exact match in terms of amplitude was not achieved. In the frequency domain, the FAS of synthetic records such as station 4404 and station 2308 are slightly higher than the observed ones. Since station 0212 did not have a Vs30 value, it was evaluated as Site C according to the regional geological classification and included in the simulation. It can be said that the synthetic records at station 0212 generally provide a good match with the observed records in both time and frequency domains.

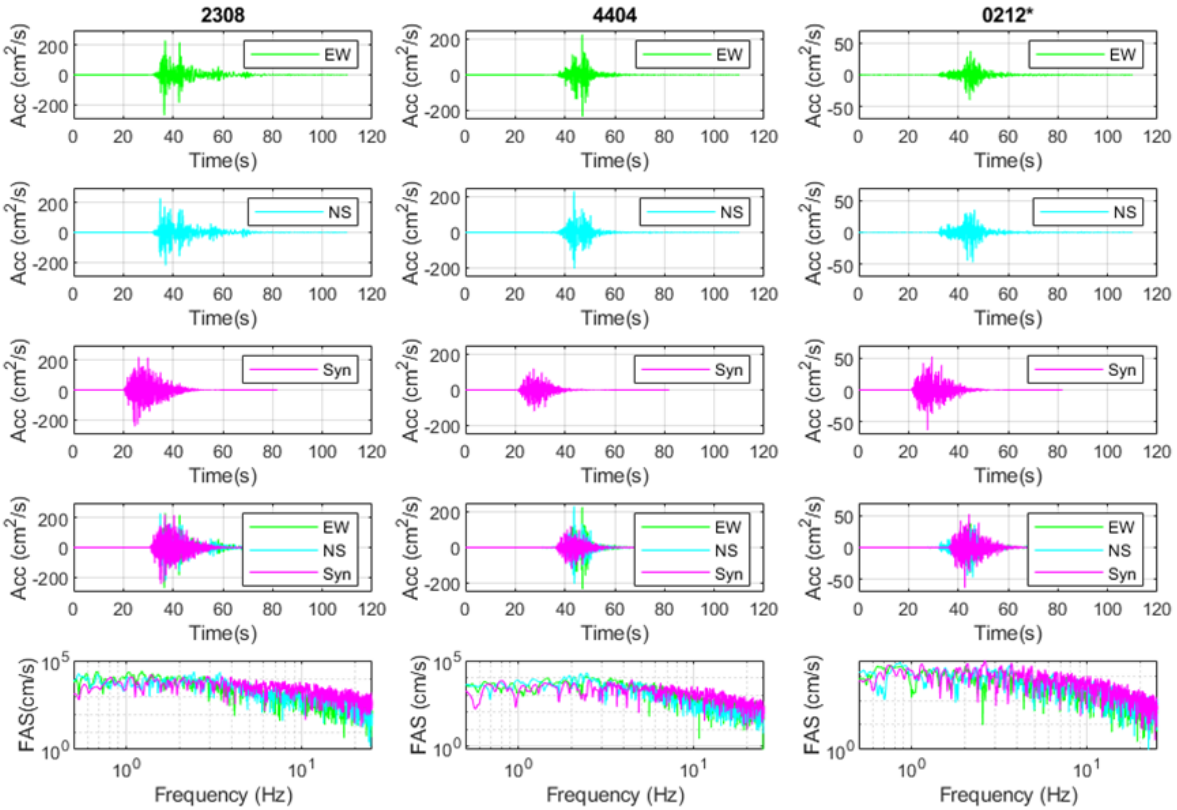

Figure 3.23. Comparison of acceleration time series and FAS of observed and simulated waveforms at stations 2308, 4404, and 0212*

Figures 3.24 and 3.25 show a comparison of stations 2301, 0204, 2302, 0205, 4401* and 2104*. In general, it can be said that the synthetic records for these 6 stations are in close agreement with the observed records. In particular, stations 2301, 0204, and 0205 showed a good match in terms of amplitude, duration and frequency content.

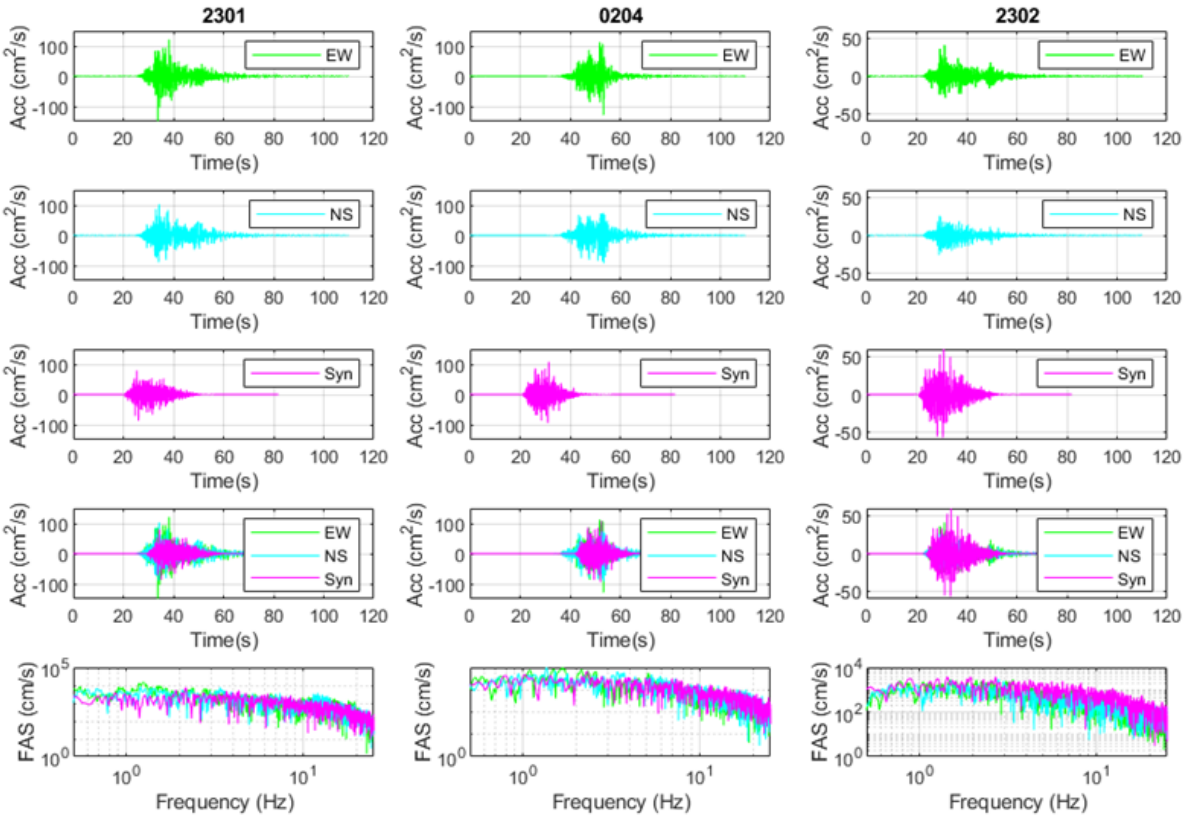

Figure 3.24. Comparison of acceleration time series and FAS of observed and simulated waveforms at stations 2301, 0204, and 2302

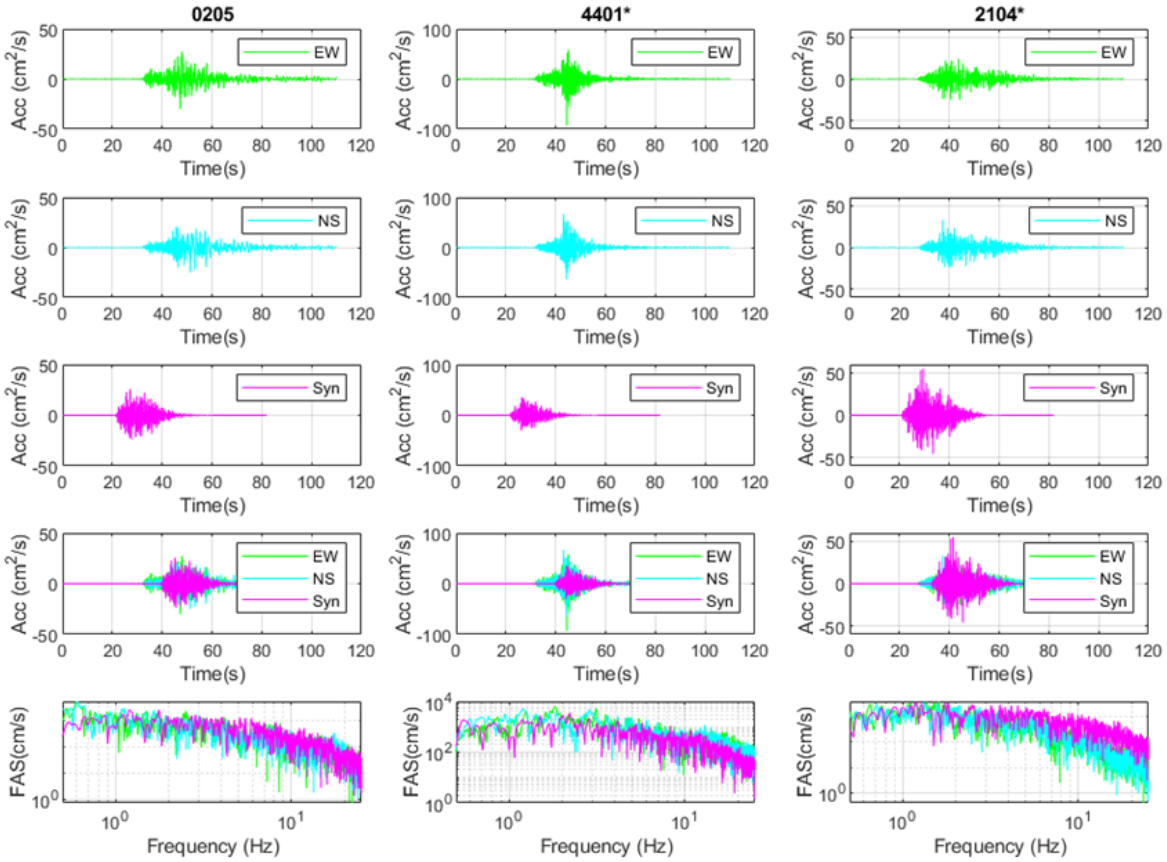

Figure 3.25. Comparison of acceleration time series and FAS of the observed and simulated waveforms at stations 0205, 4401*, and 2104*

Comparisons of simulated and real accelerations and velocities of nine stations closest to the fault rupture are shown in Figures 3.26, 3.27, and 3.28. In these figures, the green and blue curves represent the EW and NS components of recorded ground motions respectively, while the magenta curves represent the simulated motions.

Although the synthetic and observed velocities are relatively consistent in duration at stations 2308 and 4404, the amplitude values of the real records are greater than the synthetics. It can be seen that the simulations for velocity are excellent for station 0212*, both in terms of amplitude and duration.

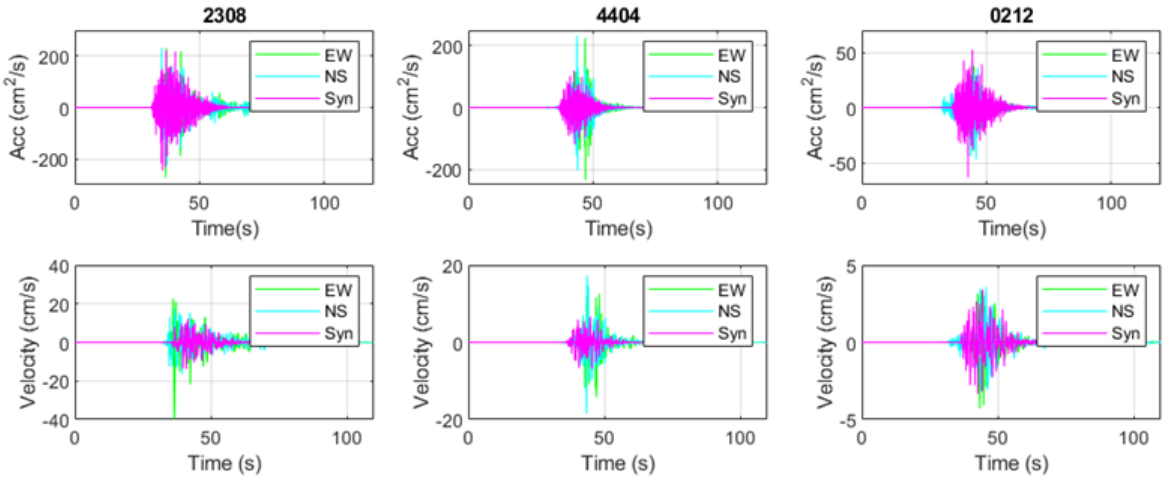

Figure 3.26. Comparison of horizontal acceleration and velocity time histories at stations 2308, 4404, and 0212*, the three closest stations to the fault rupture

When Figures 3.27 and 3.28 are examined, although the accelerations of observed and synthetic records are in harmony at stations 2301 and 0205, the observed are higher in amplitude than the synthetics in the velocity time domain. At stations 0204 and 4401, both acceleration and velocity values of the synthetic records were in good agreement with the observed records. At stations 2302 and 2104, the observed velocities are smaller than the produced.

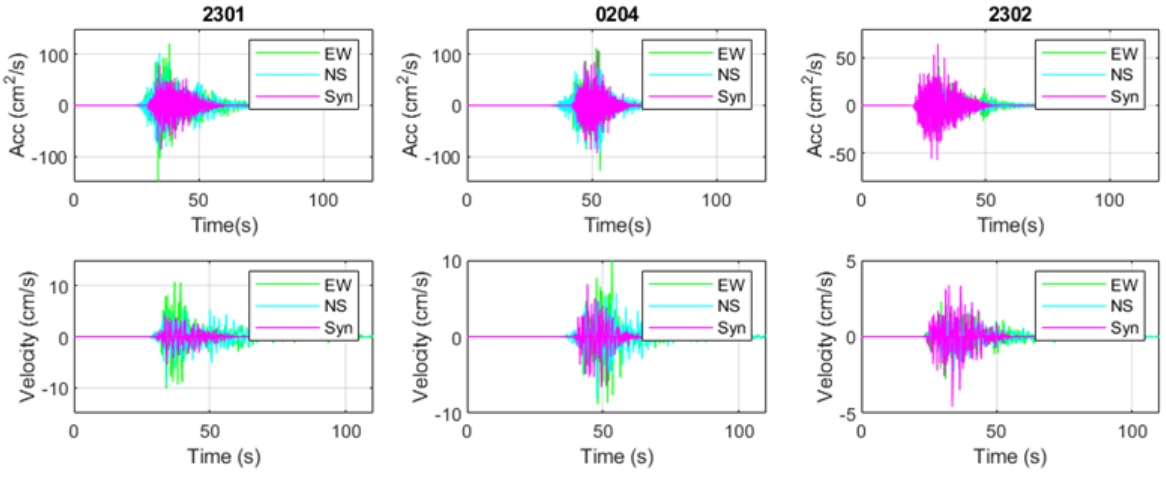

Figure 3.27. Comparison of horizontal component acceleration, and velocity time history plots at stations 2301, 0204, and 2302

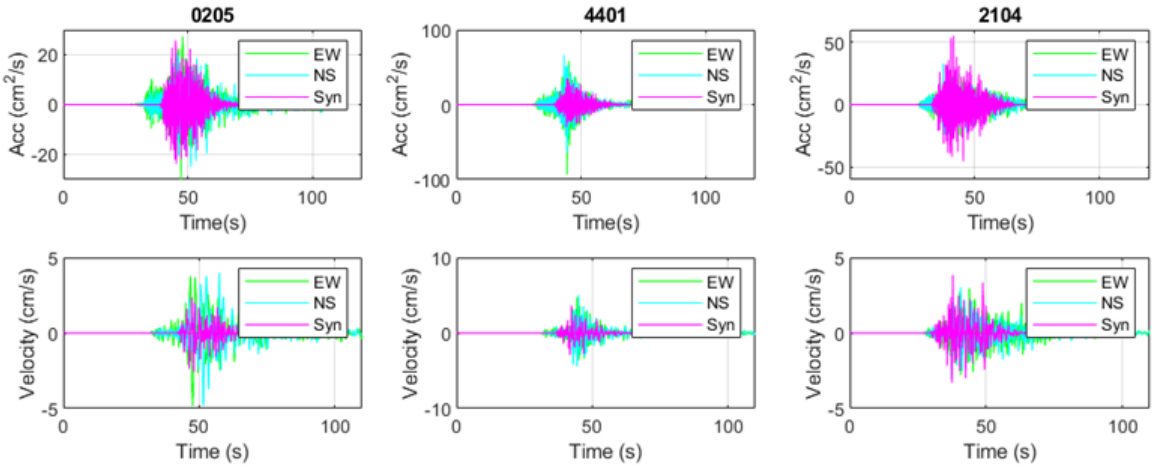

Figure 3.28. Comparison of horizontal acceleration and velocity time histories plots at stations 0205, 4401*, and 2104*

Ground motion intensity measures were investigated to compare and validate the synthetic and observed values. Initially, the comparison of the observed and synthetic peak ground accelerations and velocities against their distance from the surface rupture is shown in Figures 3.29 and 3.30 for each station.

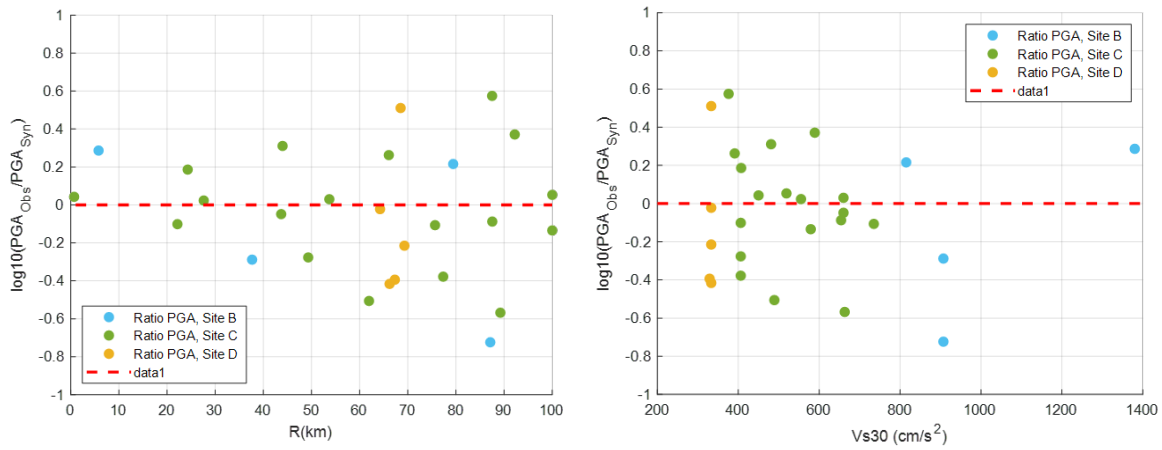

(a) (b)

Figure 3.29. The distributions of the residuals of observed and synthetic PGAs (a) versus the distance to surface rupture, (b) versus Vs30

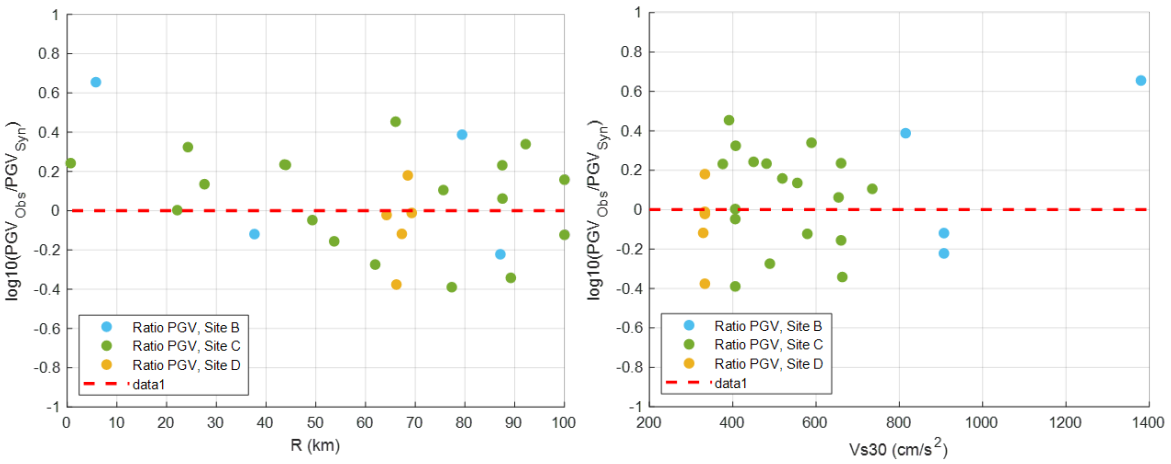

(a) (b)

Figure 3.30. The distributions of the residuals of observed and synthetic PGVs (a) versus the distance to surface rupture, (b) versus Vs30

Looking at the graphs (Figures 3.29 and 3.30), it was seen that PGA and PGV residuals did not show a systematic change with distance to the fault rupture and with Vs30. It is seen that the residuals are outside +0.5 / -0.5 range for a few stations at rupture distances larger than 60 km. Apart from these few stations, it can be said that the synthetics match the recordings (within +0.5 / -0.5) in most of the stations.

Moreover, spatial distributions of ratios of observed to synthetic PGA and PGVs are shown in Figures 3.31 and 3.32 in order to provide a better assessment of their variation with respect to their location relative to the fault rupture. The maps do not reveal any systematic variation with respect to fault rupture distance. However, in the geographical sense at stations located to the NE of the fault rupture, synthetic PGAs and PGVs are uniformly larger than the observed ones. For stations in the remaining regions, no systematic trend is evident for PGA, while the observed PGVs are generally larger than the synthetic ones.

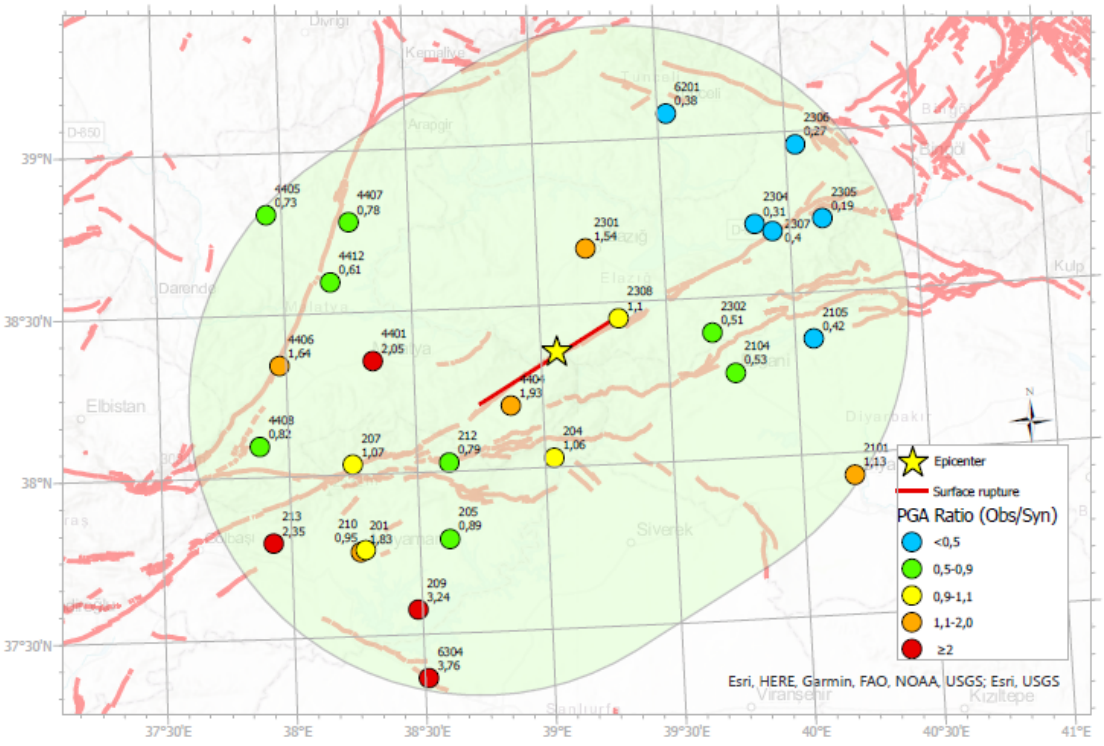

Figure 3.31. Spatial distribution of PGA ratios

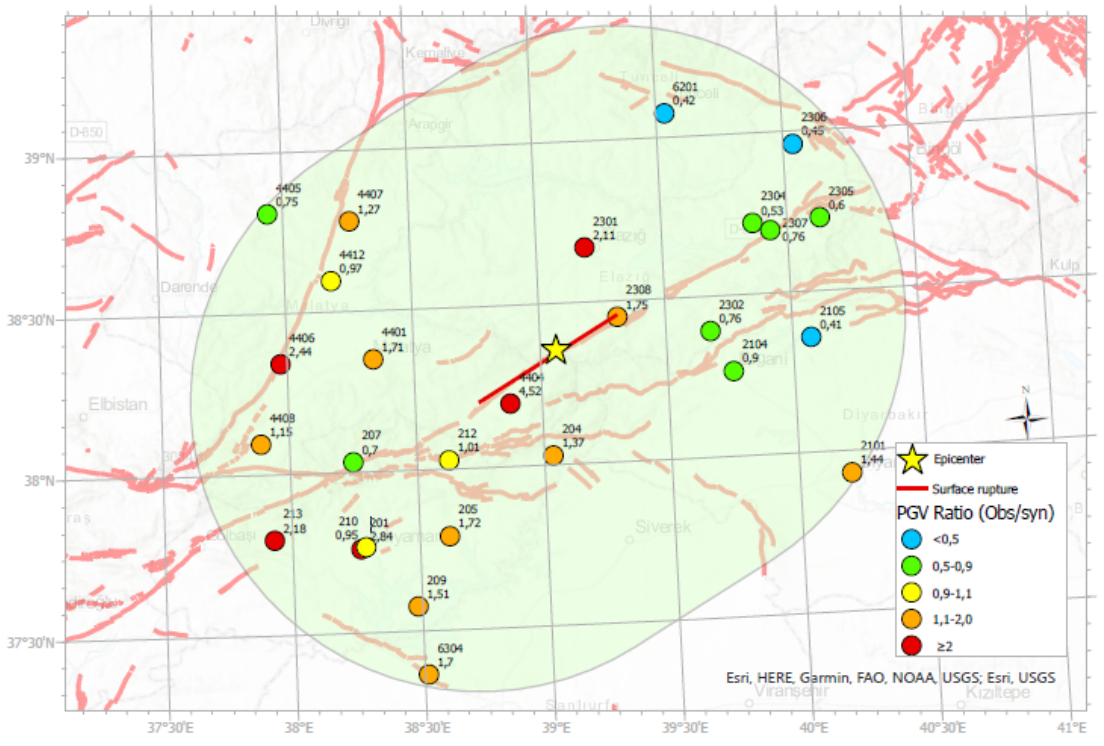

Figure 3.32. Spatial distribution of PGV ratios

3.3.4. Comparison of Observed and Synthetic Ground Motion Parameters with Ground Motion Models

In this study, comparisons were made for both observed and synthetic ground motion parameters with selected GMMs for the 24.01.2020 Mw 6.8 Elazığ earthquake. Within the scope of the study, prediction models of Boore et al. [57] (BSSA14), Chiou and Youngs [58] (CY14), Abrahamson et al. [59] (ASK14) and Kale et al. [60] (KAAH15) were used, the first three models representing global models, while the fourth one representing a local model derived based on Turkish strong ground motion data. Fault distance, earthquake magnitude, mechanism, depth, and Vs30 are the parameters used in the prediction models.

Figure 3.33 to Figure 3.36 show the PGA-Rrup (closest distance to the fault rupture) relationship graphs produced from the four GMMs for two different Vs30 values, namely 360 m/s and 760 m/s. Both observed and simulated PGA values are compared with the median and ± 1 standard deviation ranges of the predictive models.

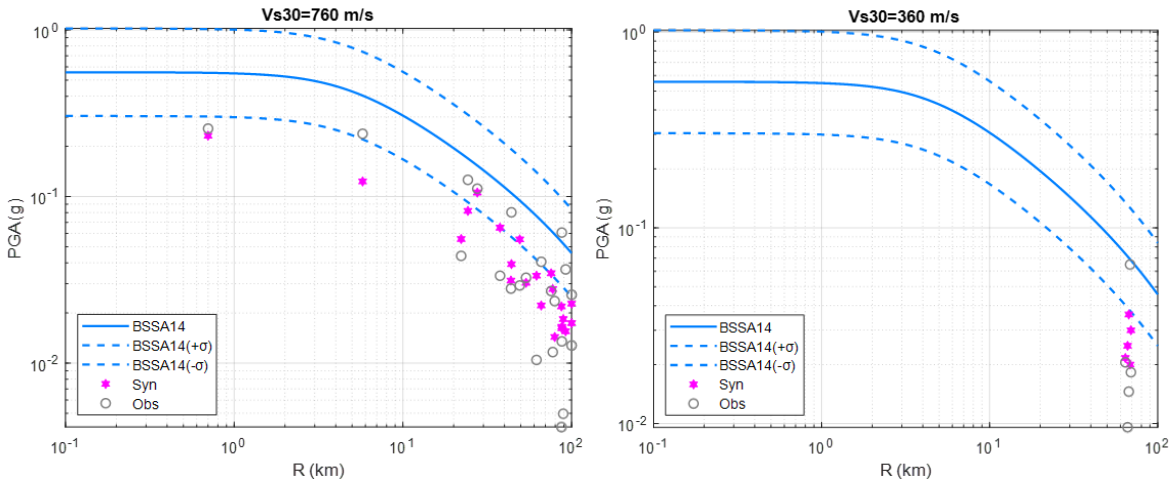

(a) (b)

Figure 3.33. Comparison of the recorded and synthetic PGAs with the BSSA14 model (a) rock site Vs30=760 m/s , (b) soil site Vs30=360 m/s

Initially, synthetic and observed (obtained as the geometric mean of the two horizontal components) PGAs for the twenty-seven stations located in an area of 100 km

radius around the fault rupture are compared with the predicted median ± 1 standard deviation values obtained by BSSA14. In this comparison, it was concluded that both synthetic and recorded PGA values were not compatible with BSSA14 estimates, as most of the stations were outside (mostly on the lower side of) the ± 1 standard deviation boundaries.

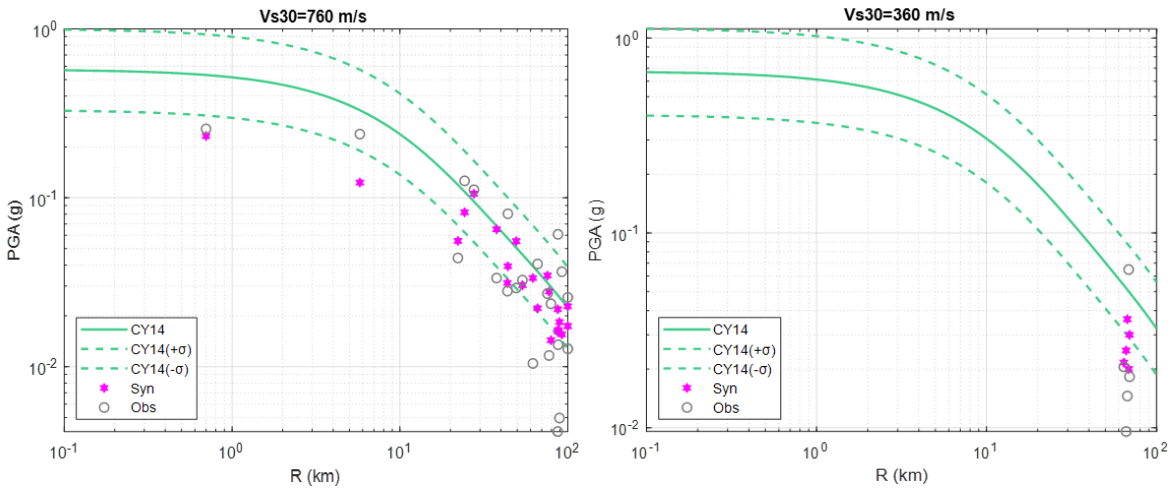

(a) (b)

Figure 3.34. Comparison of the recorded and synthetic PGAs with the CY14 model (a) rock site Vs30=760 m/s , (b) soil site Vs30=360 m/s

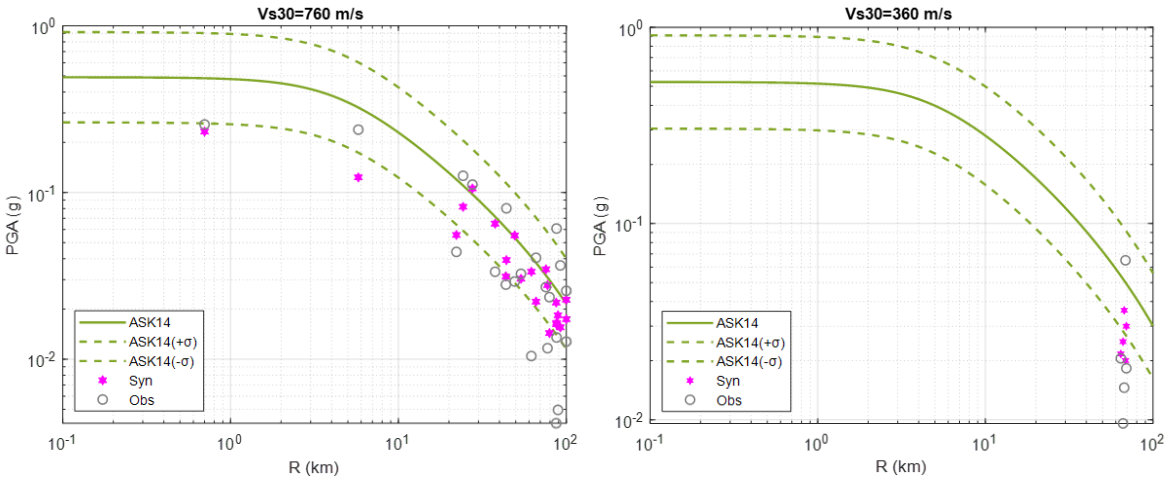

(a) (b)

Figure 3.35. Comparison of the recorded and synthetic PGAs with the ASK14 model (a) rock site Vs30=760 m/s, (b) soil site Vs30=360 m/s

Figures 3.34 and 3.35 reveal that both the simulated and recorded PGA values were generally consistent with the CY14 and ASK14 prediction models for both rock and soil stations. Most of the stations remained within ± 1 standard deviation. However, it should also be noted that the simulated ground motion amplitudes are in better agreement with the predictive models. Recorded PGA values, especially at larger distances tend to be lower than the median – 1 standard deviation values. Another interesting observation is that The PGA of the closest recording (Station 2308) obtained from this earthquake is lower than the median – 1 standard deviation value for all three predictive models mentioned above.

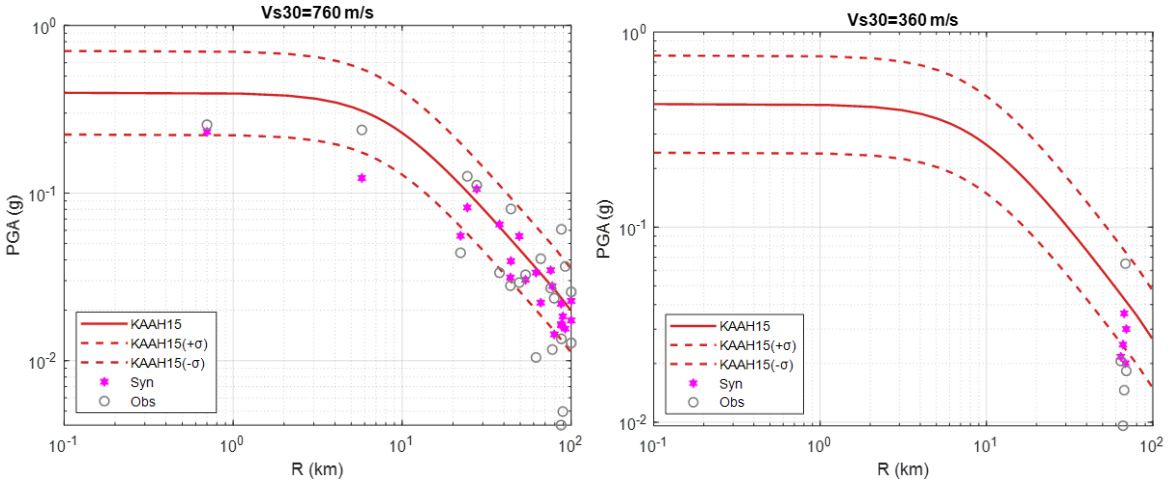

(a) (b)

Figure 3.36. Comparison of the recorded and synthetic PGAs with the KAAH15 model (a) rock site Vs30=760 m/s , (b) soil site Vs30=360 m/s

Figure 3.36 compares the recorded and synthetic PGA values with KAAH15, which is a local prediction model and it is observed that both the recorded and synthetic PGA values of station 2308, are within the prediction bounds, unlike the previous three models. Figure 3.36 shows that there is a satisfactory match between the recorded and simulated PGA values and this prediction model.

Based on all GMM comparisons, it is concluded that the CY14 and ASK14 GMM predictions agree roughly well with the simulated PGA values, while the KAAH15 prediction model gives the best results.

Figure 3.37 compares the observed and simulated PGV values with the two global models, namely CY14 and ASK14 for the VS30 values of 760 m/s and 360 m/s, while a similar comparison is provided in Figure 3.38 for the local predictive model, i.e. KAAH15.

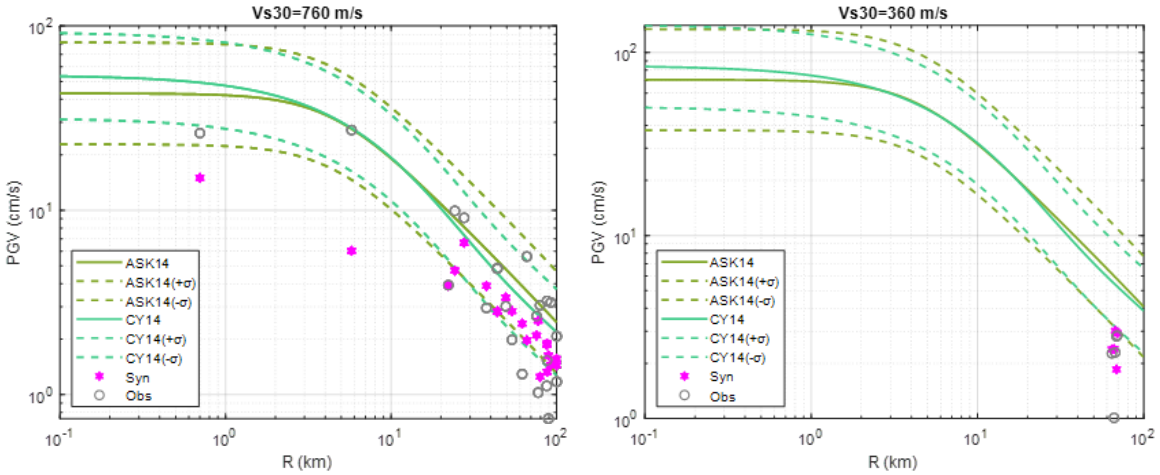

(a) (b)

Figure 3.37. Comparison of the recorded and synthetic PGVs with the CY14 and ASK14 models (a) rock site Vs30=760 m/s , (b) soil site Vs30=360 m/s

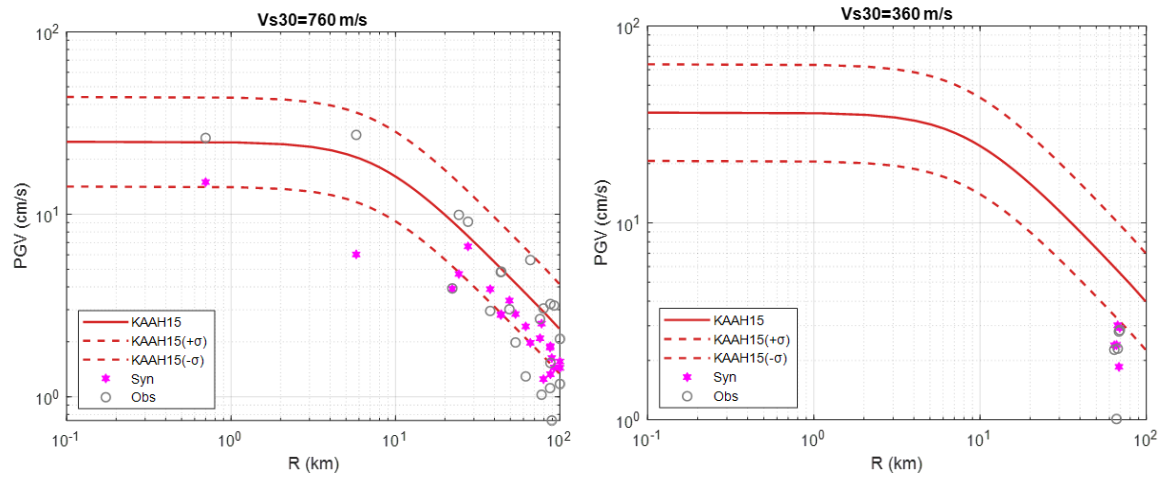

(a) (b)

Figure 3.38. Comparison of the recorded and synthetic PGVs with the KAAH15 model (a) rock site Vs30=760 m/s , (b) soil site Vs30=360 m/s

Considering the soil sites (Figures 3.37b and 3.38b) both synthetic and observed PGV values are lower than the - 1 standard deviation bound for all three models, while for the rock sites, a better agreement is observed, especially both the observed and simulated PGV values at the closest station (2308) are within the median ±1 standard deviation bound for the KAAH15 model. However, for station 4404 which is the second closest station the simulated PGV values remain lower than the - 1 standard deviation bound for all predictive models.

4. CONCLUSIONS

This thesis presents the application of the stochastic ground motion simulation methodology to the mainshock of the 24 January 2020 Elazığ-Sivrice earthquake for strong ground motion recordings within 100 km of the fault rupture. Input parameters are adopted from a study on this event [49], the models and data in previous studies suitable for the seismotectonic structure of the region.

Selected simulation model parameters are validated by comparing model bias in the frequency domain and the residuals of ground motion intensity measures (PGA and PGV) in the time domain using observed and synthetic records. As a further validation, the ground motion intensity measures associated with synthetic and observed records are compared with selected GMMs.

A simulation model was identified, the results of which yielded an optimum fit with observations in both time and frequency domains. This validated model was reached after analyzing 12 combinations of selected source, path, and site parameters and yields synthetic records for the January 24, 2020, Elazığ-Sivrice (Mw 6.8) earthquake providing a satisfactory match with real recordings. The parameters of the preferred model are presented in Table 4.1. We suggest that these parameters, specifically the path and site models, can be used in future studies on generating synthetic ground motions in eastern Türkiye.

Simulated recordings provide a reasonable match with synthetics for frequencies larger than 1 Hz. However, it should be noted that although a close agreement at frequencies larger than about 13 Hz could be achieved, at frequencies less than 13 Hz, synthetic Fourier amplitude was consistently larger than the observed ones.

Table 4.1. Parameters of the prefered simulation model

Parameter		**Value**		**References**
Source Parameter	Moment Magnitude	6.8		Afad
	Corner on upper edge of fault	38.42364 (^{o}N); 39.46586 (^{o}E)		Cheloni and Akinci [49]
	Depth of Corner on Upper Edge of Fault	0		Cheloni and Akinci [49]
	Fault Type	SS		Afad
	Strike; Dip	248; 76		Afad
	Fault Length; Fault Width	51 Km; 24 Km		Cheloni and Akinci [49]
	Subfault Length; Subfault Width	1.5 Km; 1.5 Km		Cheloni and Akinci [49]
	Slip Distribution			Cheloni and Akinci [49]
	Number of subfaults	34x16=544 subfaults		Cheloni and Akinci [49]
	Location of hypocenter within subfaults	22; 8		Cheloni and Akinci [49]
	Rupture Velocity	0.8 Beta		
	Stress Drop	7 Mpa/ 70 Bar		This study
	Pulsing Area Percentage	50 Percent		Boore [17]
	Window Function	Saragoni-Hart		Boore [7]
Path Parameter	Geometrical Spreading	$r^{-1.0}$ $r \leq 60km$		This study
		$r^{-0.5}$ $r > 60km$		
	Anelastic Attenuation (Quality Factor)	Q(f)= $180f^{0.45}$		Cheloni and Akinci [49]
	Path Duration Model	Rrup (km)	Dp (s)	Boore and Thompson [50]
		0	0	
		7	2.4	
		45	8.4	
		125	10.9	
		175	17.4	
		270	34.2	
		Slope of last segment	0.156	
	Crustal Density	2800 kg/m3		
	Crustal Shear-Wave Velocity (Beta)	3.5 kms-1		Gök et al. [51]
Site Parameter	Site Amplification	NEHRP sites		Boore and Joyner [30]
	Crustral Amplification	-		
	Kappa Factor	0.035-0.04 s		Boore and Joyner [30]

There is no evidence for a systematic dependence of simulated PGAs and PGVs on rupture distance and site class. That said, it needs to be stated that the simulated PGAs and PGVs are very close to recorded values within a rupture distance of about 60 km, as suggested by the residual analysis. For rupture distances above 60 km, the

scatter becomes larger, although still the variation could be contained within +0.6 / -0.6.

PGAs recorded during the earthquake were evaluated using the ground motion models of BSSA14, CY14, ASK14, and KAAH15. Among these models, KAAH15 was found to be the most compatible one with both observed and synthetic records of the Mw 6.8 Sivrice- Elazığ earthquake.

The findings from this study demonstrate the efficiency of the stochastic finite fault simulation method as a useful technique for generating synthetic records of earthquakes. The simulation model and its parameters developed and validated for the Elazığ (Mw 6.8) earthquake, can be further improved and used as input to other studies evaluating the seismic hazard in similar regions. In particular, the development of a geometric spreading model for rupture distances larger than 60 km, can improve the performance of the model.

The synthetic records produced can be used as inputs for various studies. It is possible to combine them with building fragility functions to estimate losses from potential earthquakes. Synthetic motions can be used to complement the datasets used to develop regional GMMs as well as in structural time history analysis.

The stochastic finite fault simulation model is successful in generating high-frequency ground motions, and the failure of synthetics to generate low-frequency content has been observed from the FAS graphs and model bias in the frequency domain in the study. However, the ground motions generated in this study through stochastic simulation can be effectively combined with long-period ground motions produced using deterministic methods. This combination provides for the creation of broadband simulations, encompassing a wide range of frequencies and providing a more comprehensive representation of seismic ground motions. The integration of both stochastic and deterministic approaches enhances the overall accuracy of the simulated ground motion fields.

REFERENCES

1. Arora, S., A. Joshi, P. Kumari and N. P. Singh, "Strong ground motion simulation techniques—a review in world context", *Arabian Journal of Geosciences*, Vol. 13, No. 14, 2020.

2. Housner, G. W., "Characteristics of strong-motion earthquakes", *Bulletin of Seismological Society of America*, Vol. 37, pp. 19–31, 1947.

3. Housner, G. W., "Properties of strong ground motion earthquakes", *Bulletin of Seismological Society of America*, Vol. 45, pp. 197–218, 1955.

4. Thomson, W. T., "Spectral aspects of earthquakes", *Bulletin of Seismological Society of America*, Vol. 49, pp. 91–98, 1959.

5. Aki, K., "Scaling law of seismic spectrum", *Journal of Geophysical Research*, Vol. 72, No. 4, pp. 1217–1231, 1967.

6. Hanks, T. C. and R. K. McGuire, "The character of high-frequency strong ground motion", *Bulletin of the Seismological Society of America*, Vol. 71, pp. 2071–2095, 1981.

7. Boore, D. M., "Stochastic simulation of high-frequency ground motions based on seismological models of the radiated spectra", *Bulletin of the Seismological Society of America*, Vol. 73, pp. 1865–1894, 1983.

8. Silva, W., "Global characteristics and site geometry", *Proceedings: NSF/EPRI Workshop on Dynamic Soil Properties and Site Characterization*, Electric Power Research Institute, EPRI NP-7337, 1991.

9. Beresnev, I. and G. M. Atkinson, "Modeling finite-fault radiation from the n spectrum", *Bulletin of the Seismological Society of America*, Vol. 87, pp. 67–84, 1997.

10. Motazedian, D. and G. Atkinson, "Stochastic Finite-Fault Modeling Based on a Dynamic Corner Frequency", *Bulletin of the Seismological Society of America*, Vol. 95, pp. 995–1010, 2005.

11. Yalcinkaya, E., "Stochastic Finite-fault Modeling of Ground Motions From the June 27, 1998 Adana-Ceyhan Earthquake", *Earth Planets Space*, Vol. 57, pp. 107–115, 2005.

12. Ugurhan, B. and A. Askan, "Stochastic Strong Ground Motion Simulation of the 12 November 1999 Düzce (Turkey) Earthquake Using a Dynamic Corner Frequency Approach", *Bulletin of the Seismological Society of America*, Vol. 100, pp. 1498–1512, 2010.

13. Karimzadeh, S., A. Askan, A. Yakut and G. Ameri, "Assessment of Simulation Techniques in Nonlinear Time History Analyses of Multi-Story Frame Buildings: A Case Study", *Soil Dynamics and Earthquake Engineering*, Vol. 98, pp. 38–53, 2017.

14. Askan, A., F. N. Sisman and B. Ugurhan, "Stochastic strong ground motion simulations in sparsely-monitored regions: A validation and sensitivity study on the 13 March 1992 Erzincan (Turkey) earthquake", *Soil Dynamics And Earthquake Engineering*, pp. 170–181, 2013.

15. Akinci, A. and A. Antonioli, "Observations and stochastic modelling of strong ground motions for the 2011 October 23 Mw 7.1 Van, Turkey, earthquake", *Geophysical Journal International*, Vol. 192, 2013.

16. Zengin, E. and E. Çaktı, "Ground Motion Simulations for the 23 October 2011 Van, Eastern Turkey Earthquake Using Stochastic Finite Fault Approach", *Bulletin of Earthquake Engineering*, Vol. 12, pp. 627–646, 2014.

17. Boore, D. M., "Comparing stochastic point-source and finite-source ground-motion

simulations: SMSIM and EXSIM", *Bulletin of the Seismological Society of America*, Vol. 99, 2009.

18. Saragoni, G. R. and G. C. Hart, "Simulation of artificial earthquakes", *Earthquake Engineering & Structural Dynamics*, Vol. 2, pp. 249–267, 1973, https://api.semanticscholar.org/CorpusID:111084303.

19. Boore, D. M., "Simulation of ground motion using the stochastic method", *Pure and Applied Geophysics*, Vol. 160, pp. 635–675, 2003.

20. Aki, K., "Attenuation of shear-waves in the lithosphere for frequencies from 0.05 to 25 Hz", *Physics of the Earth and Planetary Interiors*, Vol. 21, No. 1, pp. 50–60, 1980.

21. Haskell, N. A., "Total energy and energy spectral density of elastic wave radiation from propagating faults", *Bulletin of the Seismological Society of America*, Vol. 54, pp. 1811–1841, 1964.

22. Brune, J., "Tectonic stress and the spectra of seismic shear waves from earthquakes", *Journal of Geophysical Research*, Vol. 75, pp. 4997–5009, 1970.

23. Brune, J. N., "Correction [to "Tectonic Stress and the Spectra of Seismic Shear Waves from Earthquakes"]", *Journal of Geophysical Research*, Vol. 76, p. 5002, 1971.

24. Hanks, T. C. and H. Kanamori, "A Moment Magnitude Scale", *Journal of Geophysical Research*, Vol. 84, pp. 2348–2350, 1979.

25. Romero, S. M. and G. J. Rix, *Ground Motion Amplification in the Upper Mississippi Embayment*, Technical Report GIT-CEE/GEO-01-1, National Science Foundation Mid America Center, Atlanta, 2001.

26. Raghukanth, S. T. G. and S. N. Somala, "Modeling of Strong-Motion Data in

Northeastern India: Q, Stress Drop, and Site Amplification", *Bulletin of the Seismological Society of America*, Vol. 99, pp. 705–725, 2009.

27. Motazedian, D., "Region-Specific Key Seismic Parameters for Earthquakes in Northern Iran", *Bulletin of the Seismological Society of America*, Vol. 96, p. 1383–1395, 2006.

28. Kramer, S. L., *Geotechnical Earthquake Engineering*, Prentice Hall, Inc., Upper Saddle River, New Jersey, 1996.

29. Nakamura, Y., "A method for dynamic characteristics estimation of subsurface using microtremor on the ground surface", *Q. Rep. Railw. Tech. Res. Inst.*, Vol. 30, No. 1, 1989.

30. Boore, D. M. and W. B. Joyner, "Site amplifications for generic rock sites", *Bulletin of the Seismological Society of America*, Vol. 87, pp. 327–341, 1997.

31. Silva, W. and R. Darragh, "Engineering Characterization of Earthquake Strong Ground Motion Recorded at Rock Sites", *Electr Power Res Institute, Palo Alto, Calif.*, 1995.

32. Papageorgiou, A. S. and K. Aki, "A Specific Barrier Model for the Quantitative Description of Inhomogeneous Faulting and the Prediction of Strong Ground Motion. I. Description of the Model", *Bulletin of the Seismological Society of America*, Vol. 73, No. 3, pp. 693–722, 1983.

33. Hanks, T. C., "fmax", *Bulletin of the Seismological Society of America*, Vol. 72, pp. 1867–1879, 1982.

34. Atkinson, G. M., "Empirical Attenuation of Ground-Motion Spectral Amplitudes in Southeastern Canada and the Northeastern United States", *Bulletin of the Seismological Society of America*, Vol. 94, No. 3, pp. 1079–1095, 2004.

35. Anderson, J. and S. Hough, "A Model for the Shape of the Fourier Amplitude Spectrum of Acceleration at High Frequencies", *Bulletin of the Seismological Society of America*, Vol. 74, No. 5, pp. 1969–1993, 1984.

36. Hartzell, S., "Earthquake Aftershocks as Green's Functions", *Geophysical Research Letters*, Vol. 5, p. 14, 1978.

37. Atkinson, G. M., K. Assatourians, D. M. Boore, K. Campbell and D. Motazedian, "A Guide to Differences between Stochastic Point-Source and Stochastic Finite-Fault Simulations", *Bulletin of the Seismological Society of America*, Vol. 99, No. 6, pp. 3192–3201, 2009.

38. Hisada, Y., "Broadband strong motion simulation in layered half-space using stochastic Green's function technique", *Journal of Seismology*, Vol. 12, pp. 265–279, 2008.

39. Motazedian, D. and A. Moinfar, "Hybrid Stochastic Finite Fault Modeling of 2003, M6.5, Bam Earthquake (Iran)", *Journal of Seismology*, Vol. 10, No. 1, pp. 91–103, 2006.

40. AFAD, *24 Ocak 2020 Sivrice (Elazığ) Depremi Raporu*, Disaster and Emergency Management Authority, 2020.

41. Tatar, O., H. Sözbilir, F. Koçbulut, E. Bozkurt, E. Aksoy, S. Eski, B. Özmen, H. Alan and Y. Metin, "Surface deformations of 24 January 2020 Sivrice (Elazığ)–Doğanyol (Malatya) earthquake (Mw=6.8) along the Pütürge segment of the East Anatolian Fault Zone and its comparison with Turkey's 100-year-surface ruptures", *Mediterranean Geoscience Reviews*, Vol. 2, No. 3, pp. 385–410, 2021.

42. Bayrak, E. and C. Ozer, "The 24 January 2020 (Mw 6.8) Sivrice (Elazig, Turkey) earthquake: a first look at spatiotemporal distribution and triggering of aftershocks", *Arabian Journal of Geosciences*, Vol. 14:2445, 2021.

43. Bozkurt, E., "Neotectonics of Turkey—a synthesis", *Geodinamica Acta*, Vol. 14, pp. 3–30, 2001.

44. Emre, O., T. Y. Duman, S. Özalp, H. Elmacı, S. Olgun and F. Şaroğlu, "Açıklamalı Türkiye Diri Fay Haritası", , 2013.

45. Herece, E., *Atlas of East Anatolian Fault*, Vol. 13 of *Special Publication Series*, General Directorate of Mineral Research and Exploration, 2008.

46. Ambraseys, N. N. and J. A. Jackson, "Faulting associated with historical and recent earthquakes in the Eastern Mediterranean region", *Geophysical Journal International*, Vol. 133, pp. 390–406, 1998.

47. Seyrek, A., T. Demir, M. Pringle, S. Yurtem, R. Westway, A. Beck and G. Rowbotham, "Kinematics of the Amos Fault, southern Turkey, from Ar/Ar dating of offset Pleistocene basalt plates", *Tectonics of Strike-Slip Restraining and Releasing Bends*, Vol. 290, pp. 255–284, 2007.

48. Ambraseys, N. N., "Temporary seismic quiescence: SE Turkey", *Geophysical Journal International*, Vol. 96, pp. 311–331, 1989.

49. Cheloni, D. and A. Akinci, "Source modelling and strong ground motion simulations for the 24 January 2020, Mw 6.8 Elazığ earthquake, Turkey", *Geophysical Journal International*, Vol. 223, No. 2, pp. 1054–1068, 2020.

50. Boore, D. M. and E. M. Thompson, "Path durations for use in the stochastic-method simulation of ground motions", *Bulletin of the Seismological Society of America*, Vol. 104, No. 5, pp. 2541–2552, 2014.

51. Gök, R., M. Pasyanos and E. Zor, "Lithospheric structure of the continent collision zone: Eastern Turkey", *Geophysical Journal International*, Vol. 169, No. 3, pp. 1079–1088, 2007.

52. Akinci, A., L. Malagnini, R. B. Herrmann, N. A. Pino, L. Scognamiglio and H. Eyidogan, "High-Frequency Ground Motion in the Erzincan Region, Turkey: Inferences from Small Earthquakes", *Bulletin of the Seismological Society of America*, Vol. 91, No. 6, pp. 1446–1455, 2001.

53. Akinci, A., L. Malagnini, R. B. Herrmann and D. Kalafat, "High-frequency attenuation in the Lake Van Region, Eastern Turkey", *Bulletin of the Seismological Society of America*, Vol. 104, No. 3, 2014.

54. Akıncı, A., L. Malagnini, R. B. Herrmann, R. Gok and M. B. Sørensen, "Ground motion scaling in the Marmara region, Turkey", *Geophysical Journal International*, Vol. 166, No. 2, pp. 635–651, 2006.

55. Atkinson, G. M. and D. M. Boore, "Ground-motion relations for eastern North America", *Bulletin of the Seismological Society of America*, Vol. 85, No. 1, pp. 17–30, 1995.

56. Margaris, B. N. and D. M. Boore, "Determination of κ and β_0 from response spectra of large earthquakes in Greece", *Bulletin of the Seismological Society of America*, Vol. 88, No. 1, pp. 170–182, 1998.

57. Boore, D., J. Stewart, E. Seyhan and G. Atkinson, "NGA-West2 equations for predicting PGA, PGV, and 5% damped PSA for shallow crustal earthquakes", *Earthquake Spectra*, Vol. 30, No. 5, pp. 1057–1085, 2014.

58. Chiou, B. and R. Youngs, "Update of the Chiou and Youngs NGA model for the average horizontal component of peak ground motion and response spectra", *Earthquake Spectra*, Vol. 30, No. 3, pp. 1117–1153, 2014.

59. Abrahamson, N. A., W. J. Silva and R. Kamai, "Summary of the ASK14 ground motion relation for active crustal regions", *Earthquake Spectra*, Vol. 30, No. 3, pp. 1025–1055, 2014.

60. Kale, O., S. Akkar, A. Ansari and H. Hamzehloo, "A ground-motion predictive model for Iran and Turkey for horizontal PGA, PGV and 5response spectrum: Investigation of possible regional effects", *Bulletin of the Seismological Society of America*, Vol. 105, No. 2A, pp. 963–980, 2015.

61. Ambraseys, N. N., "The prediction of earthquake peak ground acceleration in Europe", *Earthquake Engineering & Structural Dynamics*, Vol. 24, No. 4, pp. 467–490, 1995.

62. Manning, R. and W. Campbell, "Aftershocks and duration of strong motion", *Bulletin of the Seismological Society of America*, Vol. 50, pp. 213–224, 1960.

63. Zülfikar, A. C., "24 Ocak 2020. Elazığ Depreminin Kuvvetli Yer Hareketi Verilerinin Değerlendirilmesi", *Çukurova Üniversitesi Mühendislik-Mimarlık Fakültesi Dergisi*, Vol. 35, No. 3, pp. 821–834, 2020.

64. Aki, K. and P. G. Richards, *Quantitative seismology: Theory and methods*, New York, 801, 1980.

APPENDIX A: COMPARISON OF SYNTHETIC AND OBSERVED GROUND MOTIONS IN THE TIME AND FREQUENCY DOMAIN

A.1. 24 January 2020 Elazığ-Sivrice earthquake (Mw=6.8), Site B ($760m/s < Vs30 \leq 1500m/s$)

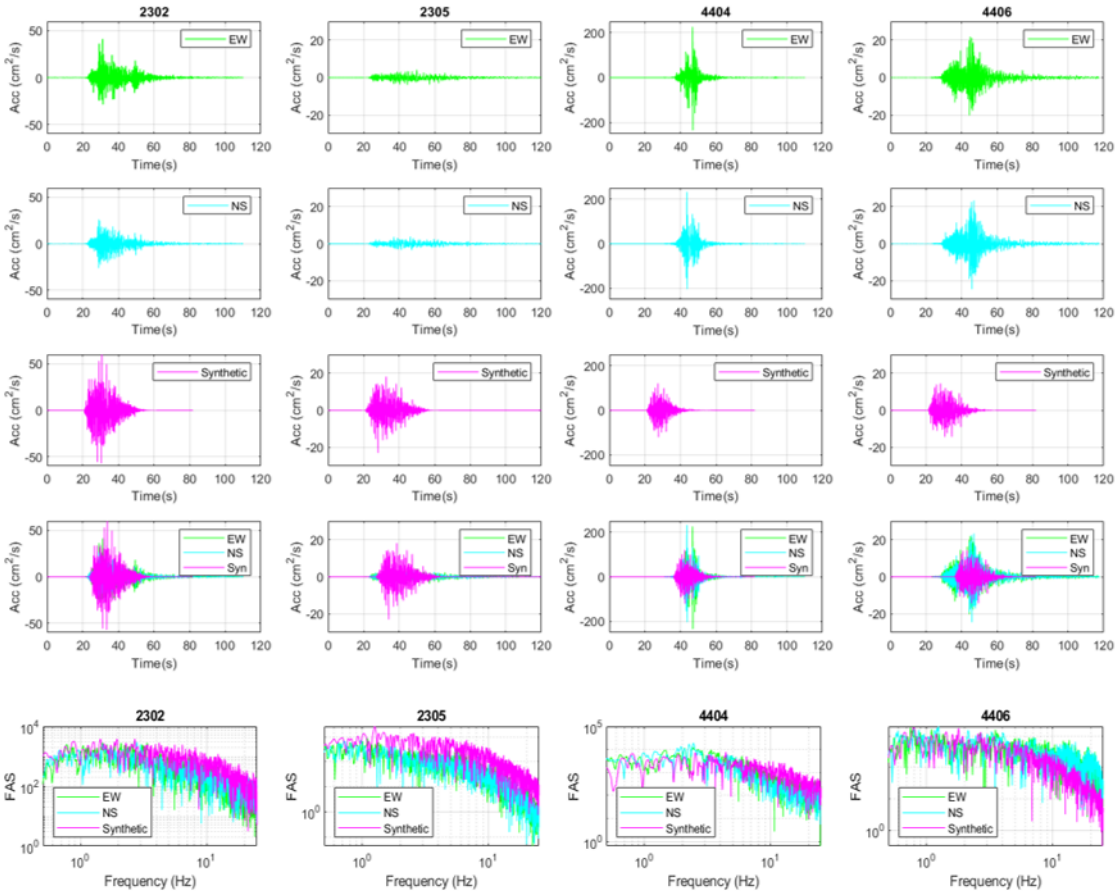

A.2. 24 January 2020 Elazığ-Sivrice earthquake (Mw=6.8), Site C ($360m/s < Vs30 \leq 760m/s$)

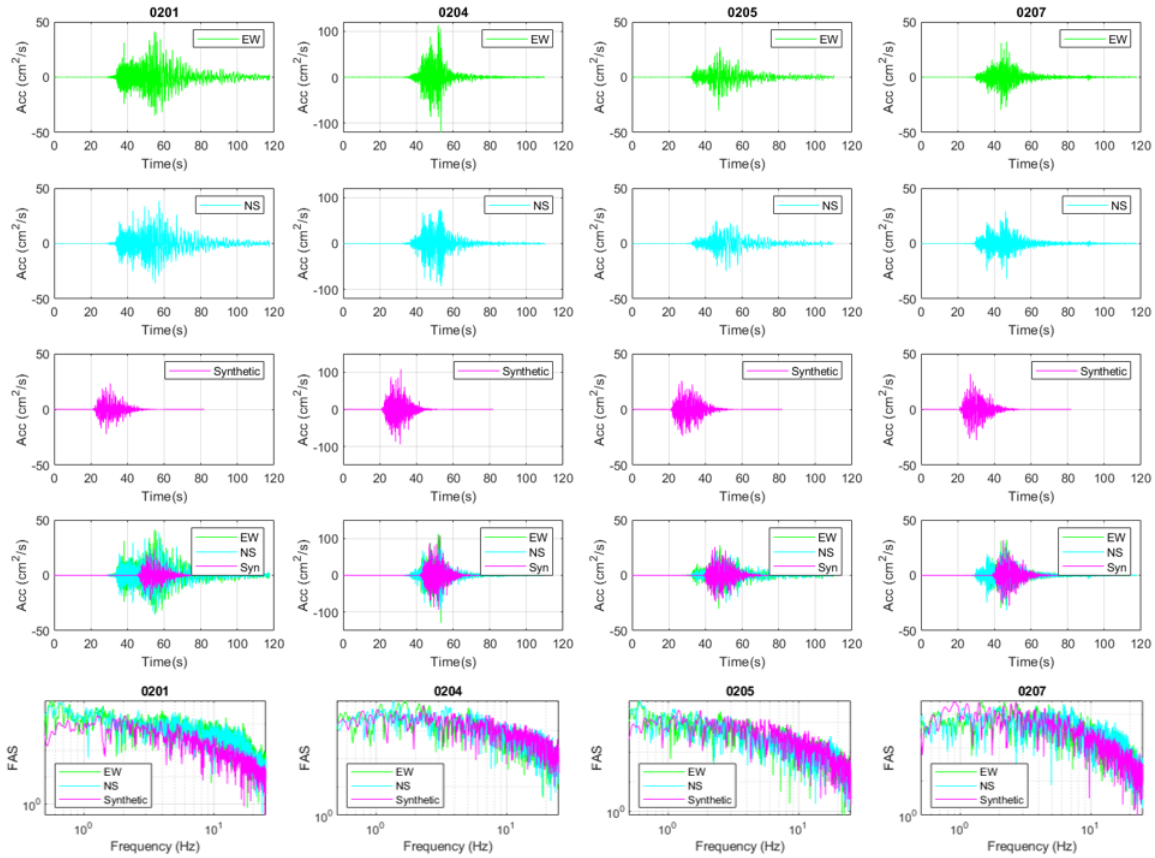

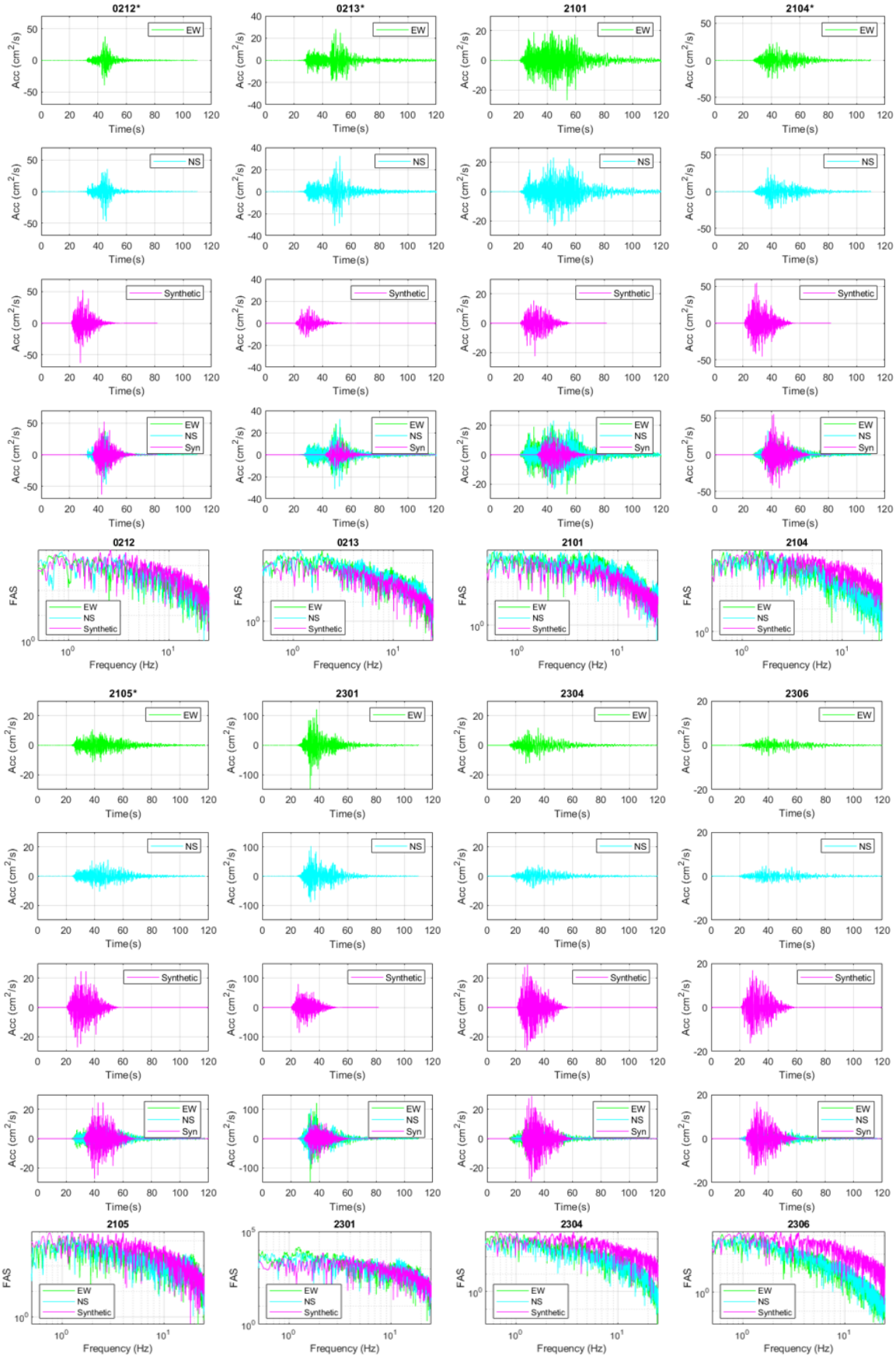
0212*
0213*
2101
2104*
EW
NS
Synthetic
Syn
Acc (cm²/s)
Time(s)
0212
0213
2101
2104
FAS
Frequency (Hz)
2105*
2301
2304
2306
2105
2301
2304
2306

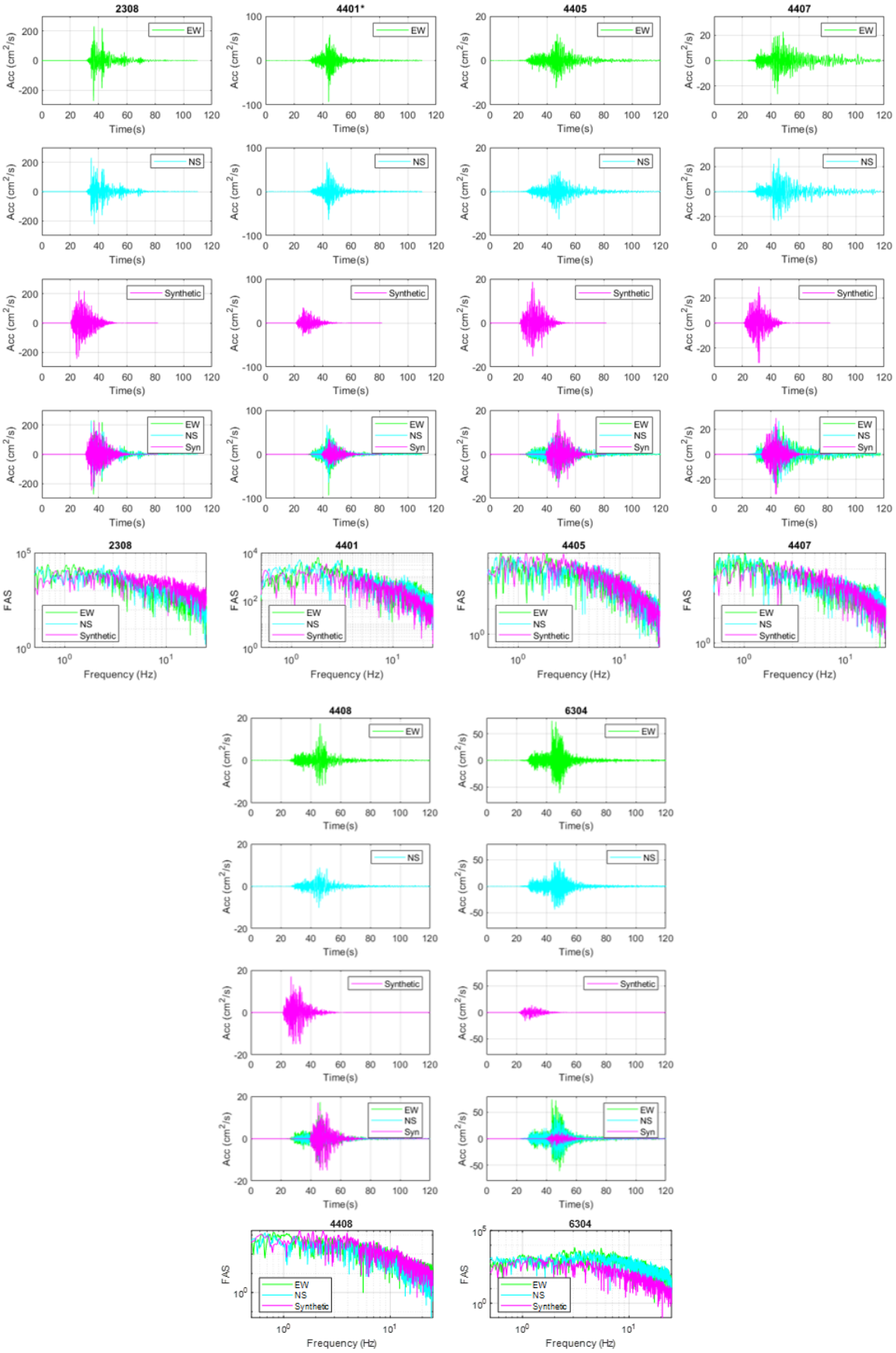
2308
4401*
4405
4407
EW
NS
Synthetic
Syn
Acc (cm²/s)
Time(s)
FAS
Frequency (Hz)
4408
6304

A.3. 24 January 2020 Elazığ-Sivrice earthquake (Mw=6.8), Site D ($180m/s < Vs30 \leq 360m/s$)

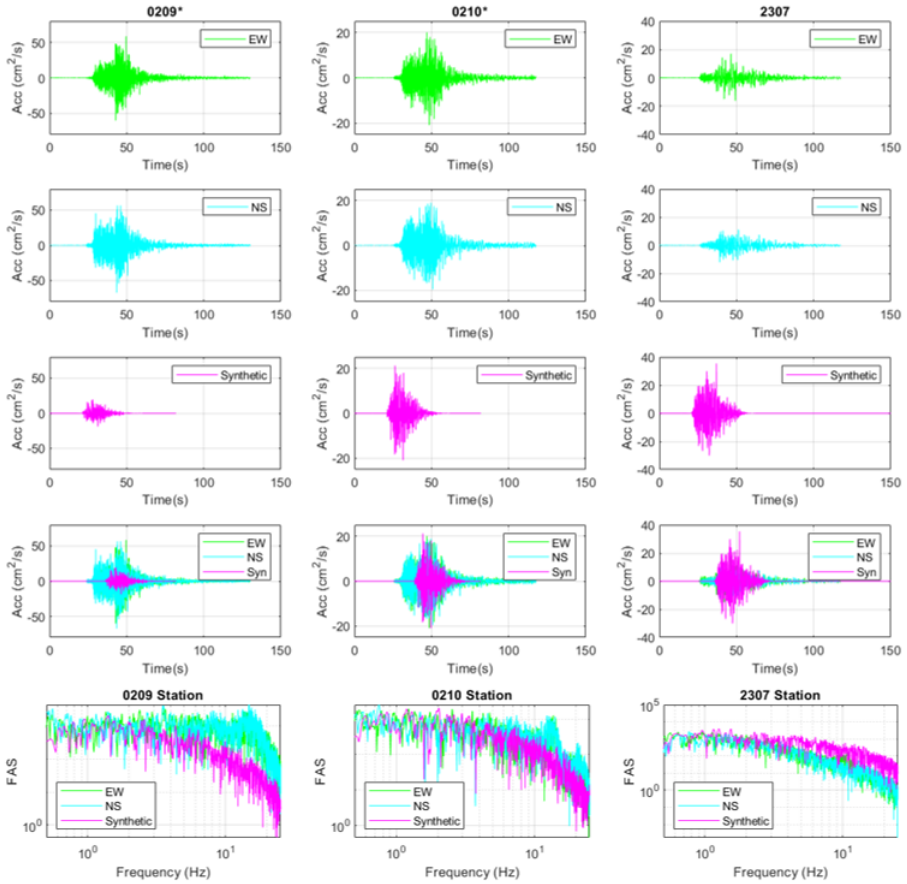

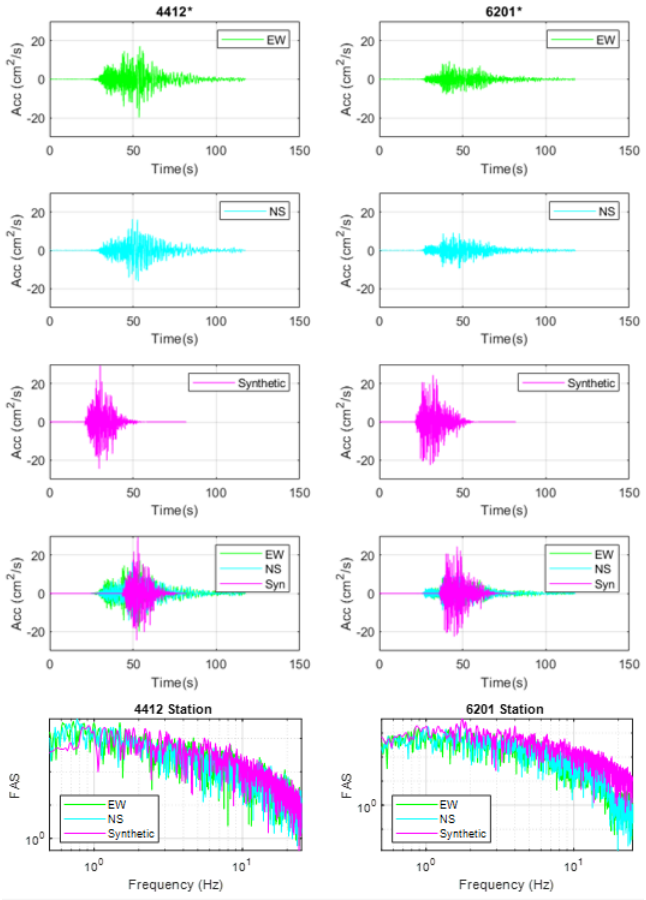
4412*
6201*
EW
NS
Synthetic
Syn
Acc (cm²/s)
Time(s)
4412 Station
6201 Station
FAS
Frequency (Hz)